AGU PUBLICATIONS

JGR

Journal of Geophysical Research: Solid Earth

RESEARCH ARTICLE

10.1002/2013JB010419

Key Points:
- New bubble dynamics model
- Developed to account for hydrodynamic interactions
- Allows to study bubble deformation and coalescence

Correspondence to:
C. Huber,
christian.huber@eas.gatech.edu

Citation:
Huber, C., Y. Su, C. Nguyen, A. Parmigiani, H. Gonnermann, and J. Dufek (2014), A new bubble dynamics model to study bubble growth, deformation, and coalescence, *J. Geophys. Res. Solid Earth*, *119*, 216–239, doi:10.1002/2013JB010419.

Received 6 JUN 2013
Accepted 13 DEC 2013
Accepted article online 27 DEC 2013
Published online 24 JAN 2014

A new bubble dynamics model to study bubble growth, deformation, and coalescence

C. Huber[1], Y. Su[1], C. T. Nguyen[2], A. Parmigiani[1], H. M. Gonnermann[2], and J. Dufek[1]

[1]School of Earth and Atmospheric Sciences, Georgia Institute of Technology, Atlanta, Georgia, USA, [2]Department of Earth Sciences, William Marsh Rice University, Houston, Texas, USA

Abstract We propose a new bubble dynamics model to study the evolution of a suspension of bubbles over a wide range of vesicularity, and that accounts for hydrodynamical interactions between bubbles while they grow, deform under shear flow conditions, and exchange mass by diffusion coarsening. The model is based on a lattice Boltzmann method for free surface flows. As such, it assumes an infinite viscosity contrast between the exsolved volatiles and the melt. Our model allows for coalescence when two bubbles approach each other because of growth or deformation. The parameter (disjoining pressure) that controls the coalescence efficiency, i.e., drainage time for the fluid film between the bubbles, can be set arbitrarily in our calculations. We calibrated this parameter by matching the measured time for the drainage of the melt film across a range of Bond numbers (ratio of buoyancy to surface tension stresses) with laboratory experiments of a bubble rising to a free surface. The model is then used successfully to model Ostwald ripening and bubble deformation under simple shear flow conditions. The results we obtain for the deformation of a single bubble are in excellent agreement with previous experimental and theoretical studies. For a suspension, we observe that the collective effect of bubbles is different depending on the relative magnitude of viscous and interfacial stresses (capillary number). At low capillary number, we find that bubbles deform more readily in a suspension than for the case of a single bubble, whereas the opposite is observed at high capillary number.

1. Introduction

Exsolved volatiles provide the driving force for explosive volcanic eruptions. While the magma is ascending to the surface, the melt becomes supersaturated with volatiles driving bubble nucleation and growth. The increasing vesicularity of the magma during decompression affects its buoyancy (provides an acceleration) and deeply affects the physical properties of the magma [*Gonnermann and Manga*, 2007]. The processes that control the nucleation and growth of gas bubbles (water and CO_2, mostly) are complex and highly nonlinear.

Bubbles gain mass by diffusion during decompression as the solubility of gas in the silicate melt is suppressed, and simultaneously, they grow by mechanical expansion due to the compressibility of the gas phase. On the other hand, the viscosity of the surrounding melt opposes a resistance to bubble growth. The interplay between diffusion of volatiles, expansion and viscous resistance during the growth of a single bubble or a periodic suspension of monodisperse bubbles in an infinite silicate melt as been studied theoretically and numerically by *Gaonac'h et al.* [1996], *Lensky et al.* [2004], *L'Heureux* [2007], *Lyakhovsky et al.* [1996], *Proussevitch et al.* [1993a], *Proussevitch and Sahagian* [1998], *Sparks* [1978], *Toramaru* [1995], and *Yamada et al.* [2008]. These studies were able to identify different growth regimes, such as viscosity and diffusion controlled, and also highlight the important effect of spatially variable viscosity and water diffusivity in these processes. Even though some of the bubble dynamics models cited above differ in terms of approaches, they share some common assumptions. The first assumption made is that bubbles have little to no hydrodynamic interactions between each other and also with rigid/partially rigid confining boundaries. In other words, bubbles remain spherical at all times, deformation between bubbles that are coupled hydrodynamically or of a bubble that interacts with a boundary (conduit wall, for example) are not taken into account. Even if the studies of *Gaonac'h et al.* [2005] and *Yamada et al.* [2008] consider the effect of coalescence into their bubble population dynamics model, it is introduced as a simple parameterization and does not account for the actual mechanics of the process.

The inability of previous bubble growth models to account for bubble deformation, coalescence, and bubble deformation under different flow environments (uniaxial decompression and shear) hampers their

©2013. American Geophysical Union. All Rights Reserved.

applicability to magmas with moderate to high vesicularities. However, the effect of bubbles on the evolution of the ascending magma increases with its vesicularity. Ultimately, prior to the onset of fragmentation, it is the rheological state and pressure distribution in a high vesicularity suspension (commonly greater than 50%) that controls the eruption dynamics [*Gonnermann and Manga*, 2003; *Proussevitch and Sahagian*, 1998; *Sparks*, 1978; *Zhang*, 1999]. In this paper, we describe a new model that is designed to investigate the physical evolution of bubble suspensions in magmas across a wide range of vesicularities (from a few to $\gg$ 50%) subjected to different decompression and shear flow conditions.

Our model differs significantly from other published bubble growth models in that it is based on a numerical approach that allows us to deal with deformed bubbles and resolves the hydrodynamical interactions between individual bubbles. In section 2, we review in greater details the existing bubble dynamics models in physical volcanology. We also discuss the advantages and limitations of our model in the light of the existing models. The physical and numerical model is presented in section 3. Model validation for the growth of bubbles by expansion and diffusion are presented in section 4. It is followed by tests of the model's ability to go beyond the limitations of existing bubble growth models. The first set of calculations consists of the ascent of a single bubble (no mass change) to a free surface and the subsequent film drainage that results in the bubble bursting at the surface. These calculations serve to calibrate a free parameter in our model, the disjoining pressure, which controls the efficiency of the drainage process, and by extension of coalescence. We use a set of experiments with an identical design to calibrate the disjoining pressure as function of the bubble Bond's number (ratio of buoyancy to surface tension stresses). The objective of the next series of calculations is to test the model accuracy with scenarios of bubble-bubble or bubble-structure interactions. We focus first on Ostwald ripening, where the thermodynamical coupling between two neighbor bubbles of different sizes leads the growth of the larger bubble at the expense of the smaller one in response to chemical potential gradients between bubbles of different sizes. Lastly, we test the model's ability to resolve accurately the viscous and capillary coupling between bubbles and the ambient melt in simple shear flow conditions. When inertia can be neglected, single bubbles are expected to reach a known steady shape (deformed when viscous stresses are important) and a known final orientation that depends on the balance between shear and capillary stresses. Finally, we use our model to study the evolution of the average deformation and orientation of bubbles in a suspension in contrast with calculations involving a single bubble. This allows us to quantify the effect of bubble-bubble hydrodynamic interactions on a sheared suspension.

2. Bubble Dynamics Models

Our understanding of bubble growth in viscous silicate melts has made significant progress over the last three decades, thanks to combined experimental [*Gardner et al.*, 2000; *Larsen and Gardner*, 2004; *Larsen et al.*, 2004; *Lyakhovsky et al.*, 1996; *Mangan and Sisson*, 2000; *Navon et al.*, 1998; *Okumura et al.*, 2006, 2008, 2009], theoretical, and numerical efforts [e.g., *Blower et al.*, 2001; *L'Heureux*, 2007; *Lensky et al.*, 2004; *Proussevitch et al.*, 1993a; *Proussevitch and Sahagian*, 1998; *Sparks*, 1978].

In this section, we present a brief overview of the field of bubble dynamics models in physical volcanology. Since the seminal work of *Verhoogen* [1951], it has been recognized that exsolved volatiles (bubbles) can play a significant role on the behavior of magmas during volcanic eruptions. Subsequently, *Sparks* [1978] developed a model of a single bubble growing in an infinite melt, where the growth of the bubble is caused by expansion and mass transfer (diffusion) during decompression and is hampered by the viscosity of the melt. The transport of dissolved volatiles to the bubble's interface was not explicitly solved for, but the growth rate due to diffusion was parameterized according to a parabolic growth law.

2.1. Population Dynamics Versus Single Bubble and Shell Models

In the late 1980s and early 1990s two different categories of multiple bubble growth models were simultaneously developed. In the first family of models, diffusion of volatiles to the bubbles is parameterized (mean-field approach), but polydispersed bubble size distribution are allowed [*Gaonac'h et al.*, 1996; *L'Heureux*, 2007; *Toramaru*, 1989, 1995; *Yamada et al.*, 2008]. These models assume that the bubbles remain spherical (no deformation), and with the exception of *Gaonac'h et al.* [2005], coalescence is not taken into account. An advantage of these models, over the second family of models discussed just below, is that they allow the inclusion of several nucleation events, although the competition for dissolved water during growth is not explicitly taken into account.

©2013. American Geophysical Union. All Rights Reserved.

The second family of models is based on the work of *Proussevitch et al.* [1993a], where the multiphase magma is represented as a monodisperse periodic array of spherical bubbles surrounded by a viscous melt shell [*Blower et al.*, 2001; *Lensky et al.*, 2004; *Lyakhovsky et al.*, 1996; *Proussevitch and Sahagian*, 1998]. This idealization was made to solve for the evolution of a single bubble-melt shell system with a radial symmetry. The model solves for the diffusive transport of dissolved volatiles to bubbles explicitly, as well as for the existence of radial gradients in water concentration and its effects on the melt viscosity and water diffusivity [*Blower et al.*, 2001; *Lensky et al.*, 2004; *Proussevitch and Sahagian*, 1998]. These models provide an accurate representation of the coupled momentum balance and diffusive transport of volatiles at the cost of an ideal geometry and a suspension that remains monodisperse at all times.

2.2. Results From Previous Studies

The two types of approaches have led to important results about the different regimes of bubble growth [*Proussevitch et al.*, 1993a; *Lensky et al.*, 2004], the effect of viscosity and diffusivity radial heterogeneities on bubble growth [*Blower et al.*, 2001; *Lensky et al.*, 2004; *Proussevitch and Sahagian*, 1998] and the effect of supersaturation on the nucleation of new bubbles and how it translates into changes in bubble number density and size distributions [*Toramaru*, 1989, 1995; *Yamada et al.*, 2008]. Nevertheless, they have been limited to low vesicularity by several assumptions. The first assumption concerns the limited hydrodynamic coupling between bubbles and between the melt and bubbles. Bubbles are not allowed to deform and remain spherical. The behavior of a bubble of radius r during shear deformation can be constrained by the capillary number

$$\mathrm{Ca} = \frac{\rho \nu \dot{\epsilon} r}{\sigma}, \tag{1}$$

where σ is the surface tension, ρ is the melt density, $\dot{\epsilon}$ is the shear rate, and ν the kinematic viscosity of the melt. At high capillary numbers ($\mathrm{Ca} > 0.1$) bubbles are expected to accommodate a large portion of the shear and the spherical assumption becomes invalid [*Manga et al.*, 1998; *Manga and Loewenberg*, 2001]. Although shear deformation of bubbles should be expected to play a significant role mostly in melts with high viscosity or for large bubbles, the hydrodynamic coupling between bubble and melt and between multiple bubbles is also expected to play a significant role in magmas with high vesicularity. The second argument that restricts the standard bubble growth models to low vesicularity is that they do not account explicitly for the competition for dissolved volatiles during the growth of bubbles of different sizes, or with different separation distances. Bubbles with different spacing, different size, and different internal pressures will be responsible for variable gradients in dissolved water content in the melt, potentially leading to implicit nonlinear interactions among neighbor bubbles. The dynamics of coalescence has been avoided, at least explicitly (besides the Smoluchowsky approach of *Gaonac'h et al.* [2005]), but it has been shown that at vesicularities of about 40%, expansion and growth can lead to significant coalescence and that this effect becomes even more important at lower vesicularity in a suspension subjected to shear [*Burgisser and Gardner*, 2004; *Okumura et al.*, 2006, 2008]. Another implicit assumption common to all previous models is that there is no respective motion between the center of mass of a bubble and the ambient melt. This is a good approximation for small bubbles and melts with high viscosity, but it is expected to break down in the other cases or when connected pathways start to form between coalesced bubbles and gas-melt segregation occurs.

2.3. Motivation for the New Heterogeneous Bubble Dynamics Model

In this study, we develop a new bubble dynamics model to overcome the aforementioned limitations of existing models. The aim of this model is to keep an explicit description of the mass transport of dissolved water by diffusion in the melt, but without the restriction of radial symmetry and the assumption of limited bubble interactions. In other words, the new model provides the ability to solve for bubble deformation and coalescence. In addition, we are able to consider enough randomly distributed bubbles to track the evolution of polydisperse bubble size distributions. Finally, the new model allows us to investigate the effect of an imposed shear rate on the rheological behavior of the suspension and on the bubbles coalescence rate by solving for the finite and spatially variable motions between each bubble's center of mass on the melt surrounding bubbles.

©2013. American Geophysical Union. All Rights Reserved.

Before describing the new model in detail, we list some of the present (should be overcome in future studies) and absolute limitations of our model.

1. The model is discretized in space on a homogeneous grid; it is therefore not accurate in terms of water concentration profile at the early stage of degassing. The model of *Proussevitch et al.* [1993a] is expected to yield more accurate results at low vesicularity. However, at later stages, when the vesicularity is greater and the diffusion profile less steep, the accuracy of the diffusion model will be much improved, because it is accurate to the second order in space. Although the spatial resolution is an issue for the accuracy of the diffusion model at early times, we want to emphasize that film drainage between bubbles and coalescence, which are solved by a Volume-of-Fluid method (see below), use a mass balance description that has a subgrid spatial resolution.
2. The model is, as of now, limited to 2-D calculations. An extension to 3-D is not trivial (calculation time) but nothing should prevent it in the near future. Although the existing models discussed above are intrinsically 3-D, they assume a perfect radial symmetry and therefore reduce the physics to 1 dimension.
3. In this study, water-dependent melt viscosity and diffusivity were not taken into account. We plan on addressing this issue in a future study. There are no formal limitations regarding heterogeneous viscosity and diffusivity in the lattice Boltzmann method, because the relaxation times for the discrete Boltzmann equations that represent momentum and mass conservation can be varied locally without any subsequent change in the algorithm.

3. Numerical Method

The lattice Boltzmann method (LBM) has emerged as an efficient alternative to traditional Computational Fluid Dynamics solvers and was developed as an extension to cellular automata [*Frisch et al.*, 1986; *Higuera et al.*, 1989]. The LBM solves for the evolution of particle distribution functions according to simple rules and follows a discretized form of Boltzmann's kinetic equation. The model we use for bubble dynamics is an extension of the model proposed by *Koerner et al.* [2005] where the fluid inside bubbles is assumed inviscid and interfaces between the two fluids are treated as a free surface boundary condition. In this section, we describe the model and introduce some of the extensions that were required to adapt it to decompression and shear flow conditions.

3.1. The Lattice Boltzmann Model for Free Surfaces

The lattice Boltzmann free surface method on which our bubble model is based has been used successfully by different authors to measure dynamic contact angles and study metal foaming processes and free surface flows [*Attar and Koerner*, 2009; *Koerner et al.*, 2005]. Within the LBM, Boltzman's equation is commonly discretized in physical and velocity spaces so that particle distribution functions, at a given lattice site, can stream along a finite number of directions (lattice velocity vectors) and reach a neighbor site at the next time step. In general, in 2-D, a topology with one rest velocity $\mathbf{e}_0 = (v_{x,0} = 0, v_{y,0} = 0)$ and eight finite velocity vectors connecting the site to its nearest neighbors is used. This nine velocity lattice topology is usually referred to as the D_2Q_9 lattice (see Figure 1a) with velocities $\mathbf{e}_i$

$$\mathbf{e}_i = \begin{cases} (0,0) & \text{if } i = 0 \\ \left(\cos\left(\frac{(i-1)\pi}{2}\right), \sin\left(\frac{(i-1)\pi}{2}\right)\right) & i = 1, \ldots 4 \\ \left(\cos\left(\frac{(2i-1)\pi}{4}\right), \sin\left(\frac{(2i-1)\pi}{4}\right)\right) & i = 5, \ldots 8. \end{cases} \tag{2}$$

The evolution equation for the particle distribution functions f_i (where i stands for the discrete velocity vector along which the particles are moving) uses a linearized collision operator, often referred to as the BGK [*Bhatnagar et al.*, 1954] or single relaxation time operator [*Qian et al.*, 1992]. The update of the distribution between two consecutive time steps (t and $t + 1$) is given by

$$f_i(\mathbf{x} + \mathbf{e}_i, t + 1) = f_i(\mathbf{x}, t) + \frac{1}{\tau_F}[f_i^{\mathrm{eq}}(\mathbf{x}, t) - f_i(\mathbf{x}, t)] + F_i, \tag{3}$$

where $\mathbf{x}$ are the spatial coordinates on the lattice, t is time, f_i^{eq} is the equilibrium distribution (defined below), and F_i represents a body force acting on the distribution f_i. The relaxation time τ_F is explicitly related to the kinematic viscosity of the fluid

$$\nu = c_s^2\left(\tau_F - \frac{1}{2}\right), \tag{4}$$

©2013. American Geophysical Union. All Rights Reserved.

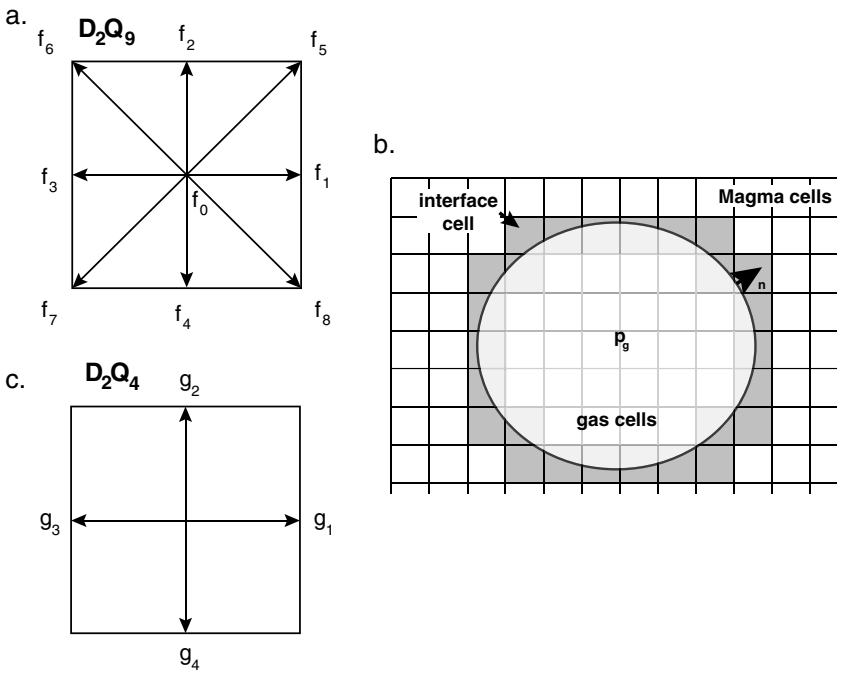

Figure 1. Discretization of the particle distribution functions in velocity space. The two choices of lattice used (a) for the viscous fluid flow around bubbles (D_2Q_9) and (c) for the advection-diffusion equation for the dissolved volatile concentration (D_2Q_4). (b) An illustration of the Volume-of-Fluid approach used for the lattice Boltzmann free surface model is shown. The domain is divided among three cell types: bubble cells where no dynamics is computed, melt/fluid cells where Navier-Stokes and the advection-diffusion equations are solved, and interface cells that separate the other two types and act as boundary conditions between bubbles and ambient melt.

where c_s^2 is a constant of the lattice (one third on the D_2Q_9). The local fluid density and momentum (and hence velocity) can be retrieved as moments of the particle distribution functions

$$\rho(\mathbf{x},t)=\sum_{i=0}^{8} f_i \quad \text{and} \quad \rho(\mathbf{x},t)\mathbf{u}(\mathbf{x},t)=\sum_{i=0}^{8}\mathbf{e}_i f_i. \tag{5}$$

The equilibrium distribution is a quadratic function of the local fluid velocity and depends linearly on the density

$$f_i^{\mathrm{eq}}(\mathbf{x},t)=w_i\rho(\mathbf{x},t)\left[1+\frac{\mathbf{u}\cdot\mathbf{e}_i}{c_s^2}+\frac{1}{2}\frac{(\mathbf{u}\cdot\mathbf{e}_i)^2}{c_s^4}-\frac{1}{2}\frac{\mathbf{u}\cdot\mathbf{u}}{c_s^2}\right], \tag{6}$$

where w_i are the lattice weights, $w_0=\frac{4}{9}$, $w_{1-4}=\frac{1}{9}$, and $w_{5-8}=\frac{1}{36}$. This generic model was shown to recover the Navier-Stokes and the continuity equations with second-order accuracy in space and first-order accuracy in time [*Higuera et al.*, 1989; *Qian et al.*, 1992]. For simplicity, we subdivide equation (3) into two steps: the collision step

$$f_i^{\mathrm{out}}(\mathbf{x},t)=f_i(\mathbf{x},t)+\frac{1}{\tau_F}[f_i^{\mathrm{eq}}(\mathbf{x},t)-f_i(\mathbf{x},t)]+F_i, \tag{7}$$

and the streaming step

$$f_i^{\mathrm{in}}(\mathbf{x}+\mathbf{e}_i,t+1)=f_i^{\mathrm{out}}(\mathbf{x},t). \tag{8}$$

The free surface model developed by *Koerner et al.* [2005] uses an approach similar to the Volume-of-Fluid method, where a continuous scalar occupancy field m allows to track the position and evolution of the interface between two fluids (here bubble and silicate melt). The lattice is divided among three cell types: gas, melt, and finally interface cells (see Figure 1b). The type of each cell is updated dynamically according to the

©2013. American Geophysical Union. All Rights Reserved.

local evolution of the scalar quantity m. The field variable m represents the fluid mass content of the cell and is given by

$$m(\mathbf{x},t)=\begin{cases}0 & \text{if } \mathbf{x}\in \text{ gas cell}\\ \rho(\mathbf{x},t) & \text{if } \mathbf{x}\in \text{melt cell}\\ \rho(\mathbf{x},t)\epsilon(\mathbf{x},t) & \text{if } \mathbf{x}\in \text{ interface cell.}\end{cases} \tag{9}$$

where ϵ is the volume fraction of melt at site $\mathbf{x}$ and time t (between 0 and 1). An evolution equation for the distribution of each cell type is required because bubbles and melt can move with respect to the lattice, while simultaneously bubbles can expand and grow. The evolution equation for m follows the procedure described in *Koerner et al.* [2005] and consists of tracking the mass exchange between neighbor sites of each cell type

$$\Delta m_i(\mathbf{x},t)=\begin{cases}0 & \text{if } \mathbf{x}\in \text{gas cell}\\ \Delta f_i^{\text{out}}\equiv f_i^{\text{out}}(\mathbf{x}+\mathbf{e}_i,t)-f_i^{\text{out}}(\mathbf{x},t) & \text{if } \mathbf{x}\in \text{ melt cell}\\ \frac{1}{2}(\epsilon(\mathbf{x},t)+\epsilon(\mathbf{x}+\mathbf{e}_i,t))\Delta f_i^{\text{out}} & \text{if } \mathbf{x}\in \text{interface cell.}\end{cases} \tag{10}$$

where $\mathbf{e}_i=-\mathbf{e}_i$. *Koerner et al.* [2005] showed that this scheme conserves mass locally and that m can now be updated at each site using

$$m(\mathbf{x},t+1)=m(\mathbf{x},t)+\sum_{i=0}^{8}\Delta m_i(\mathbf{x},t). \tag{11}$$

Obviously, the mass content of each cell must stay bounded $0<m(\mathbf{x},t)<\rho(\mathbf{x},t)$, which is enforced by imposing the following set of rules: if $m\geq\rho$, the cell is converted to a melt cell; if $m<0$, then it is converted to a gas (bubble) cell. Similarly, new interface cells are created when a former melt cell evolves so that $m<\rho$ or when the mass content of a gas cell becomes greater than 0 ($m>0$). A more complete description of the mass redistribution algorithm can be found in *Koerner et al.* [2005].

Because the viscosity ratio between the melt and the gas bubbles is generally greater than 10^7, we assume that the bubbles are inviscid. That allows us to treat the effect of bubbles on the melt as boundary conditions similar to free surfaces, i.e., no tangential stress, but existing pressure drop at the interface between the two fluids caused by interfacial tension and density difference between the two fluids. If the gas pressure is known, we can apply a pressure boundary condition on the melt. We assume that the gas within the bubble behaves ideally

$$p_g=\frac{nRT}{V}, \tag{12}$$

where n is the number of moles of gas molecules in a given bubble, V its volume, T the ambient temperature (here assumed constant), and R the ideal gas constant.

In the free surface algorithm, the effect of the bubble at the interface with the melt is an imposed pressure boundary condition. At any given interface cells, some elements f_i of the particle distribution functions are missing because they carry information from a gas cell (outside of the domain where the f_i's are defined) to the interface cell. These missing distributions are reconstructed to impose the correct boundary condition on the melt, using information from the gas pressure in the bubble and the curvature of the interface at the interface site. For more details about this procedure, the reader is referred to *Koerner et al.* [2005].

The effect of surface tension σ between gas and melt can be added to the gas-interface boundary conditions as

$$p_g(\mathbf{x},t)=\frac{n(t)RT}{V(t)}-2\kappa(\mathbf{x},t)\sigma, \tag{13}$$

where $n(t)$ and $V(t)$ are the number of moles of gas molecules (here we focus on water) and the volume of the bubble, respectively, and $\kappa(\mathbf{x},t)$ is the local curvature of the interface. When considering multiple bubbles interacting with each other, or the interaction of a bubble with a free surface, an additional term is included in the pressure boundary condition

$$p_g(\mathbf{x},t)=\frac{n(t)RT}{V(t)}-2\kappa(\mathbf{x},t)\sigma-\Pi, \tag{14}$$

©2013. American Geophysical Union. All Rights Reserved.

which is the disjoining pressure Π. The disjoining pressure is defined as the variation of Gibbs free energy with distance associated with the interaction of two melt-gas interfaces associated with different objects (e.g., two different bubbles or a bubble and a free surface)

$$\Pi = -\frac{1}{A}\left(\frac{\partial G}{\partial x}\right), \tag{15}$$

where A is the surface area of the interacting surfaces and G is the Gibbs free energy. The disjoining pressure has a fundamental impact on controlling the coalescence rate between bubbles and therefore the stability of suspensions. For simplicity, the disjoining pressure can be taken as a linearly decreasing function of the distance between the two interacting objects with a finite range d_{range}

$$\Pi(d_{\text{int}}) = \begin{cases} 0 & \text{if } d_{\text{int}} \geq d_{\text{range}} \\ c_{\Pi}|d_{\text{int}} - d_{\text{range}}| & \text{if } d_{\text{int}} < d_{\text{range}}. \end{cases} \tag{16}$$

The disjoining pressure is therefore set by two constants: its amplitude c_{Π} and range d_{range}, as well as the distance between the two interacting interfaces neighbor objects d_{int}.

We discuss how the disjoining pressure model is calibrated from experiments in section 4. We note, however, that keeping track of the mass content in each interface nodes allows us to accurately model the coalescence of bubbles (if the disjoining pressure term is correctly calibrated) which occurs when the fluid content of the interface node separating to adjacent bubbles has fully drained out of the interface. Finally, for all calculations involving solid surfaces, the contact angle between the interface separating the two fluid phases and the solid boundaries is such that the gas phase is nonwetting.

3.2. Decompression Scheme

During volcanic eruptions, decompression exerts a major control on the physical state of the magma. The change in pressure influences the density of the gas phase and also the solubility of the volatile species dissolved in the melt. A large number of experiments were designed to study the growth regime of suspensions under different decompression conditions, from a static decompression (instantaneous pressure drop) to constant decompression rates [*Burgisser and Gardner*, 2004; *Gardner et al.*, 1999, 2000; *Larsen and Gardner*, 2000]. While many of these studies focused on the transition from equilibrium to nonequilibrium bubble growth, as function of imposed decompression rates and melt viscosity [*Gardner et al.*, 1999, 2000; *Navon et al.*, 1998], other studies investigated the effect of bubble-bubble interactions on the growth rate of a suspension [*Larsen and Gardner*, 2000], the vesicularity at the onset of coalescence [*Burgisser and Gardner*, 2004; *Larsen et al.*, 2004], and the effect of shear on coalescence and the formation of outgassing permeable pathways [*Okumura et al.*, 2009].

During decompression, two processes lead to bubble growth: (1) mechanical expansion (no mass exchange between the melt and the suspension) and (2) degassing by diffusion from a supersaturated melt to adjacent bubbles. In this section, we focus first on mechanical expansion. In order to account for decompression, we modified the scheme presented above to allow for the pressure in the gas phase to evolve in response to the change of ambient pressure. We assume a pressure reference frame where the pressure in the ambient melt p_{amb} (which is supposed to follow closely the decompression pressure path) is constant over a given run. In that reference frame, the pressure inside bubbles is expected to increase if the decompression rate is fast enough for the growth of the bubble to be impeded by the viscous melt. Assuming a decompression rate in the melt $(\mathrm{d}p/\mathrm{d}t)_{\text{dec}}$ (< 0 for decompression), the pressure evolution in bubbles does not follow equation (12), but rather

$$\frac{\mathrm{d}p_g}{\mathrm{d}t} = RT\left[\frac{1}{V}\frac{\mathrm{d}n}{\mathrm{d}t} - \frac{n}{V^2}\frac{\mathrm{d}V}{\mathrm{d}t}\right] - \left(\frac{\mathrm{d}p}{\mathrm{d}t}\right)_{\text{dec}}, \tag{17}$$

where the number of moles of gas n is allowed to evolve with time (in the case of exsolution). The volume of gas in a bubble V can change in response to mechanical expansion and if n increases by diffusion of water from the melt. The effect of surface tension and the disjoining pressure can be added into the boundary condition similarly to equation (14). In the limit where diffusion of dissolved water is neglected, the pressure evolution reduces to

$$\frac{\mathrm{d}p_g}{\mathrm{d}t} = -RT\frac{n}{V^2}\frac{\mathrm{d}V}{\mathrm{d}t} - \left(\frac{\mathrm{d}p}{\mathrm{d}t}\right)_{\text{dec}}, \tag{18}$$

©2013. American Geophysical Union. All Rights Reserved.

where the pressure equilibrium between the melt and the bubbles (no residual overpressure) is reached when the volume change of bubbles accommodates all the decompression of the modeled magma parcel, which occurs only when the growth of bubbles is not viscously limited.

Although not the focus of this paper, the decompression model presented here does not restrict us from studying the effect of nonuniform decompression rates. Equation (17) can limit the choice of time steps (small time steps) for large decompression rates, as the pressure in the bubble must remain > 0. However, the scheme was found to be stable over the whole range of calculations presented in this study.

3.3. Volatile Diffusion and Bubble Growth

In order to allow for the degassing of dissolved volatiles, the model needs to account for diffusion of dissolved volatiles in the melt. We use a similar approach to *Koerner et al.* [2005], where a second set of distribution functions g_j is used to model an advection-diffusion equation with imposed concentration boundary conditions at the bubble-melt interfaces. Because the advection-diffusion equation requires less symmetry than the momentum conservation in the lattice Boltzmann method, we use a different lattice topology with four velocities (D_2Q_4, see Figure 1c). The lattice nodes for g_j coincide with the D_2Q_9 lattice used for the flow calculations. A similar discretized Boltzmann equation can be solved for the dissolved volatile concentration

$$g_j(\mathbf{x}+\mathbf{e}_j, t+1) = g_j(\mathbf{x}, t) + \frac{1}{\tau_G}[g_j^{eq}(\mathbf{x}, t) - g_j(\mathbf{x}, t)], \tag{19}$$

where the velocity index $j = 1, \ldots, 4$ (see equation (2)). The relaxation time τ_G is related to the diffusion coefficient of the dissolved volatiles in the melt

$$D_{H_2O} = c_{sG}^2\left(\tau_G - \frac{1}{2}\right), \tag{20}$$

and the constant $c_{sG}^2 = \frac{1}{2}$ for the D_2Q_4 lattice. The local dissolved water content is retrieved from the distribution with

$$C(\mathbf{x}, t) = \sum_{j=1}^{4} g_j(\mathbf{x}, t), \tag{21}$$

and the equilibrium distribution is given by

$$g_j^{eq}(\mathbf{x}, t) = w_{j,G} C(\mathbf{x}, t)\left(1 + \frac{\mathbf{e}_j \cdot \mathbf{u}}{c_{sG}^2}\right), \tag{22}$$

where the velocity $\mathbf{u}$ is obtained from the Navier-Stokes solver (from the distributions f_i), $w_{j,G} = \frac{1}{4}$ for $i = 1, \ldots, 4$ are the lattice weights for the distributions g_j corresponding to the four discrete velocity vectors $\mathbf{e}_j$ which point East-North-West-South (see Figure 1). The equilibrium distributions are therefore a function of the local flow velocity and the local concentration only. The water dependence of the diffusivity can be easily included in the model by setting the relaxation time τ_G to be a function of the dissolved water content C. This effect will not be explored here but will be part of a subsequent study. This lattice Boltzmann model for advection diffusion was shown to recover the advection-diffusion equation [*Suga*, 2006]

$$\frac{\partial C}{\partial t} + \mathbf{u} \cdot \nabla C = \nabla \cdot \left(D_{H_2O} \nabla C\right). \tag{23}$$

We impose the dissolved water content in the melt at a bubble-melt boundary to follow Sievert's law

$$C_b(\mathbf{x}, t) = S\sqrt{p_g}, \quad \mathbf{x} \in \text{Interface cell} \tag{24}$$

with S the Sievert's constant and p_g the bubble's pressure [*Burnham*, 1975; *Sparks*, 1978]. This boundary condition at the interface site is imposed by setting the missing distributions (coming from the adjacent gas cell) g_x to

$$g_x = g_x^{eq}(C_b, \mathbf{u}) + g_{\bar{x}}^{eq}(C_b, \mathbf{u}) - g_{\bar{x}}(C_b, \mathbf{u}), \tag{25}$$

while the other g_j's are set to $g_j(C_b, \mathbf{u})$. In equation (25), the overbar defines the opposite velocity direction, e.g., $\bar{\text{North}} = \text{South}$. The bubble model, including the diffusion of the dissolved volatiles, at the exception of the decompression scheme, has been validated in previous studies [*Koerner et al.*, 2005].

©2013. American Geophysical Union. All Rights Reserved.

To allow for degassing and bubble growth during decompression, the decompression rate $(\mathrm{d}p/\mathrm{d}t)_{\mathrm{dec}}$ should be included into the advection-diffusion scheme for dissolved water in the melt. As the pressure exerts only a second-order effect on the diffusivity of dissolved water in the melt, we will not consider this effect here. Following the decompression scheme described above, where the pressure reference frame follows the pressure of the ambient melt, the decompression rate is expected to play a role in the solubility of water at the bubble-melt interface. We therefore introduce the decompression of the suspension into our boundary condition with

$$C_b(\mathbf{x}, t) = S\sqrt{p_g + \int_0^t \left(\frac{\mathrm{d}p}{\mathrm{d}t}\right)_{\mathrm{dec}} \mathrm{dt}}. \tag{26}$$

A first note concerns the sign of $(\mathrm{d}p/\mathrm{d}t)_{\mathrm{dec}}$; because it is negative, the decompression term leads to a decrease in solubility with time. However, if the bubble growth is limited by the viscosity of the ambient melt, the overpressure buildup in the bubble in response to the decompression can ideally compensate for the decompression of the magma, and in that particular case, the solubility of water at the bubble interface should remain constant as is expected from the expression above.

4. Validations

A detailed description of benchmark problems solved with the generic free surface lattice Boltzmann model can be found in *Koerner et al.* [2005]. Here we focus on validations of our model compared to analytical solutions (expansion) and published experimental and numerical results of single bubble growth to test our decompression scheme.

4.1. Single and Multiple Bubble Growth by Expansion During Decompression

The following calculations are meant to test if the pressure evolution equation (equation (17)) allows us to solve for the expansion of a bubble or a bubble suspension (up to 120 different bubbles) during a constant decompression rate experiment, in the absence of degassing (no diffusion growth). All the runs presented here use similar initial conditions, we normalize pressure with regard to the initial ambient pressure $p_{\mathrm{amb}}(t = 0) = 1$, and start with $N = 1, 5, 40$, and 120 bubbles with a given initial radius r_0 (initially monodisperse size distribution). The physical domain can be decomposed in two main regions, the suspension (melt + bubbles) that occupies the lower half and a free surface with a fictitious atmosphere in the upper half. The presence of the free surface and atmosphere is required to allow for the suspension to expand (increase in volume). Besides the top free surface, the whole domain is bounded by solid walls. In all the following calculations, we use a constant decompression rate with a duration Δt (5000 time steps in our simulation) so that

$$\left(\frac{\mathrm{d}p}{\mathrm{d}t}\right)_{\mathrm{dec}} \Delta t = -\frac{3}{4}\, p_{\mathrm{amb}}(t = 0). \tag{27}$$

For a single bubble, we should therefore expect the final volume of the bubble to be 4 times greater than its initial volume, given that enough time is allowed for the bubble-melt system to relax to a new steady state. In Figure 2, we show the evolution of a single bubble during a decompression experiment, where the decompression lasts for half of the calculation time of 5000 time steps. Starting with N bubbles, each with an initial volume V_0 and a volume of melt (incompressible and constant) V_m, we get by mass conservation

$$\frac{NV_0}{NV_0 + V_m} = C\frac{4 \times NV_0}{4 \times NV_0 + V_m}, \tag{28}$$

where C is the expansion factor and V_m can be calculated from the vesicularity ϕ of the suspension at $t = 0$. We can compare the value of C obtained theoretically with equation (28) with the ratio of final to initial suspension vesicularity in our calculations. In Table 1, we use the initial volume fraction of bubbles to compute the theoretical expansion factor and final vesicularity. These results are then compared graphically with the time series of increasing vesicularity obtained numerically with our decompression model (see Figure 3). We observe in all cases, even when coalescence is prominent (the run containing initially 120 bubbles reaches a steady state with 29 bubbles), an excellent agreement between the numerical model and theory. Because coalescence is not significant for the final steady state vesicularity of a decompressed suspension, we used an arbitrary value for the constant c_{Π}, which controls the amplitude of the disjoining pressure term. In the following calculations, the coalescence rate becomes important and we will calibrate the disjoining pressure constant value with laboratory experiments.

©2013. American Geophysical Union. All Rights Reserved.

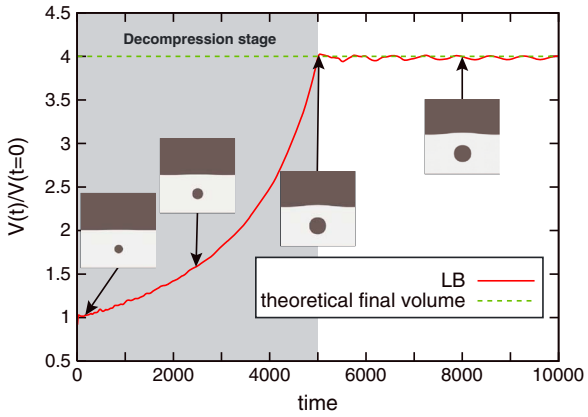

Figure 2. Linear decompression of a bubble. The decompression phase lasts for 5000 iterations. Here only mechanical expansion is allowed (no diffusion) and the bubble reaches its final expected size (see dashed line) after decompression. The oscillations observed around the steady state are caused by capillary waves generated at the free surface by the growth of the bubble during the decompression phase.

4.2. Growth of a Single Bubble

An empirical test for our model is to reproduce the qualitative features observed in other numerical models and laboratory experiments during the growth of a single bubble by diffusion and expansion during a linear decompression event. First, when the bubble is small and the diffusive flux of water to the bubble interface can be neglected, the growth of the bubble is delayed [*Lensky et al.*, 2004; *Liu and Zhang*, 2000; *Proussevitch et al.*, 1993a; *Proussevitch and Sahagian*, 1998; *Sparks*, 1978]. *Lensky et al.* [2004] showed that under this growth regime (often referred to as viscous-limited growth regime), the bubble radius grows exponentially and the argument of the exponential growth depends on the timescale for viscous relaxation t_{visc} and the timescale for decompression t_{dec}

$$\frac{R(t)}{R_i} = \exp\left(\frac{t*^2}{2}\frac{t_{dec}}{t_{vis}}\right), \tag{29}$$

where $t* = |dp/dt|t$,

$$t_{vis} = \frac{4\mu}{p_i} \tag{30}$$

and

$$t_{dec} = \frac{p_i}{|dp/dt|}. \tag{31}$$

Here the subscript i refers to an initial condition (prior to decompression), p_i the initial ambient melt pressure, and μ is the dynamical viscosity of the melt, assumed to be constant. In Figure 4, we show the volume and radial growth of the bubble obtained with our model. The insets correspond to snapshots taken at different times during the growth. We observe an early exponential growth stage that is consistent with the time-delay process observed in other numerical models [*Lensky et al.*, 2004; *Liu and Zhang*, 2000; *Proussevitch et al.*, 1993a; *Proussevitch and Sahagian*, 1998]. As the bubble grows, the growth regime changes and displays the usual sigmoidal radius growth observed in other models [*Proussevitch et al.*, 1993a; *Proussevitch and Sahagian*, 1998].

Table 1. Summary of Results From the Decompression of a Bubble Suspension

$N(t=0)$	$\phi(t=0)$	$N(\Delta t)$	C Theory	C Calculated	$\phi(t=\Delta t)$
1	0.019	1	4	4	0.076
5	0.0099	5	3.08	3.11	0.0308
40	0.077	27	3.27	3.273	0.252
120	0.22	29	2.42	2.418	0.532

©2013. American Geophysical Union. All Rights Reserved.

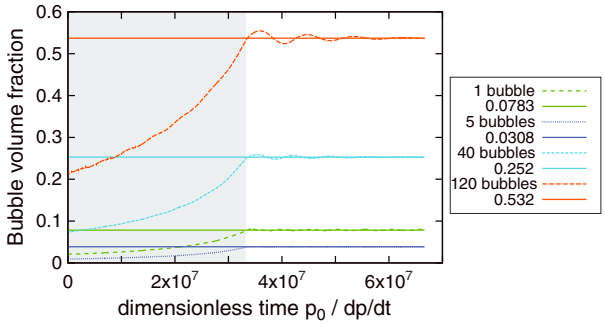

Figure 3. Same exercise as for Figure 2 but with a different amount of bubbles. It is interesting to note that the runs at higher vesicularity hosted a large amount of coalescence, but it did not affect the accuracy of the decompression scheme.

5. Bubble-Bubble Interactions

The interaction between bubbles in a suspension is highly nonlinear and has been neglected in existing bubble dynamics models in physical volcanology. The focus of our model is to account for these nonlinear interactions between bubbles under a range of realistic magmatic conditions. In this section, we demonstrate the ability of the model to treat bubble thermodynamic and hydrodynamic interactions during diffusion (Ostwald ripening), deformation, and coalescence.

5.1. Diffusion and Ostwald Ripening

In a polydisperse bubble suspension diffusion coarsening, often referred to as Ostwald ripening, can lead to the growth of large bubbles at the expense of smaller ones [*Lautze et al.*, 2011], because the growth of large bubbles is thermodynamically more favorable due to surface energy. A similar process is known to operate during the growth of crystals in magmatic and high temperature metamorphic environments [*Nemchin et al.*, 2001; *Park and Hanson*, 1999].

This coarsening process was first recognized by *Ostwald* [1897], but it took about 60 years to establish a theory that yields quantitative predictions. The physics underlying the coarsening is simple: because of surface tension, small bubbles have a higher gas pressure than larger ones. In fact, assuming static conditions the difference in pressure between two spherical bubbles with radius r_1 and r_2 is

$$\Delta p = p_1 - p_2 = 2\sigma\left(\frac{1}{r_1} - \frac{1}{r_2}\right). \tag{32}$$

The pressure difference increases with bubble volume differences and surface tension. The diffusion of dissolved water from a small to a large bubble is caused by the pressure dependence of the solubility condition at the bubble-melt interface

$$C_1 = S\sqrt{p_{\text{amb}} + \frac{2\sigma}{r_1}} \tag{33}$$

$$C_2 = S\sqrt{p_{\text{amb}} + \frac{2\sigma}{r_2}}. \tag{34}$$

If $r_1 < r_2$, then $C_1 > C_2$ and water will diffuse from the small to the large bubble, further increasing the capillary pressure difference and the coarsening process. The development of analytical models with predictive capabilities is, however, not simple.

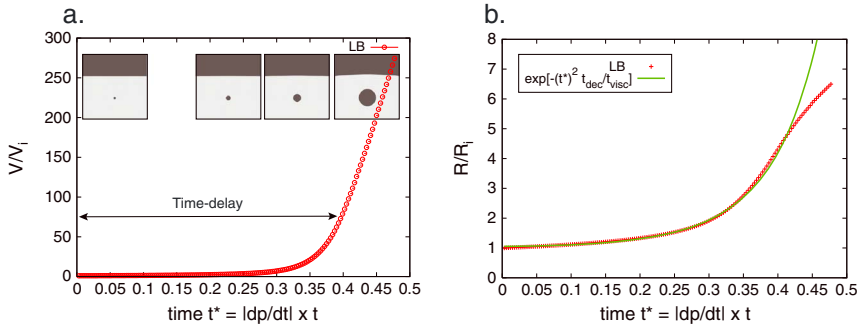

Figure 4. Illustration of the growth of a bubble by a combination of mechanical expansion and diffusion during decompression. (a) The inset illustrates the size of the growing bubble and shows clearly the time delay caused by the viscosity of the ambient melt at the onset of the growth. (b) A fit of our results with the exponential growth derived for early growth by *Lensky et al.* [2004] is shown.

©2013. American Geophysical Union. All Rights Reserved.

A major difficulty for modeling this process arises from the boundary conditions, the concentration of dissolved water changes over time and so does the position of the two boundaries as one bubble shrinks and the other grows. The first predictive models were based on highly idealized bubble population statistics, such as the LSW model developed by *Lifshitz and Slyozov* [1961] and *Wagner* [1961]. These models assumed that the bubble remains spherical at all time and, more importantly, that the suspension is dilute so that the interaction between bubbles could be replaced by a mean-field interaction. These models predict that, during steady coarsening, the average bubble radius increases with time$^{1/3}$ for diffusion-controlled growth. Recently, more sophisticated models of population dynamics emerged, like the model of *DeHo* [1991] where the mean-field approximation was replaced by a nearest-neighbor interaction. Theoretical models of transient coarsening still require a large number of simplifying assumptions and a theoretical model that allows to account qualitatively for Ostwald ripening processes remains challenging.

For magmatic suspensions, *Mangan et al.* [1993] and *Mangan and Cashman* [1996] discussed vesicle size distributions (VSDs) in basaltic magmas, erupted either effusively or explosively. Although the importance of diffusive coarsening was not directly measured in the skewed VSDs, the faster diffusion and also broader range of radii among coexisting bubbles make basaltic magmas more prone to efficient diffusion coarsening.

Estimates of the duration for the diffusive exchange of water between bubbles separated by a melt film was discussed by Proussevitch and coworkers, using some important assumptions such as steady state diffusion and simple geometry [*Proussevitch et al.*, 1993b]. Under these assumptions, they anticipated that the radius of the shrinking bubble decreases with the square root of time. This model does not take into account the change in film thickness that is expected to happen during the process. *Lautze et al.* [2011] presented laboratory experiments to study Ostwald ripening in magmas with different compositions (mafic andesite to rhyolite). They showed that, in agreement with a multitude of other laboratory experiments, the temporal evolution of the bubble's radius expected from the LSW theory is not obtained. They concluded that transient coarsening with widely variable growth rates was more susceptible to be relevant during fast degassing events such as during the ascent of bubbles in a volcanic conduit.

Available bubble growth models in physical volcanology cannot account for diffusive coarsening, because these models either assume that the suspension is monodispersed (no gradients of solubility) or because they do not solve explicitly for volatile diffusion around individual bubbles [*Gaonac'h et al.*, 1996; *Toramaru*, 1995; *Yamada et al.*, 2008]. Recently, *Yamada et al.* [2008] expanded on the polydispersed model of *Toramaru* [1995] and introduced a critical radius below which bubbles were made to disappear to the benefit of larger bubbles. To a first order, they argued that the forced disappearance of bubbles smaller than this critical radius could account for Ostwald ripening, but the process is not explicitly solved for. In realistic scenarios at high vesicularity, it is likely that the coarsening of a volcanic foam can involve more than two adjacent bubbles of different sizes.

Our model allows us to model diffusive coarsening, because we can solve explicitly for the dynamics of multiple bubbles with various sizes and for water diffusion from and to neighboring bubbles. In Figure 5, we show an attempt of modeling Ostwald ripening, where two bubbles of different initial sizes ($r_1 = 7$ and $r_2 = 30$ grid spacing) are initially separated by four lattice nodes. The large bubble is initially in chemical equilibrium with the host melt. While the smaller bubble loses water over time by diffusion, the pressure and temperature remain fixed during this run. Although a comparison of the model with an analytical or asymptotical solution remains mostly qualitative, this calculation highlights the potential of the method to resolve complex thermodynamical interactions between neighbor bubbles. As we expect, the total volume/mass of exsolved volatiles remains constant throughout the run (dotted line in the two upper panels), but the volume of the small bubble decreases with time while the larger bubble grows.

Assuming steady state diffusion, bubble growth in melt has been shown to follow a parabolic growth rate $r^2 \propto t$. Similarly, the diffusive exchange of water across a melt film separating two close bubbles of different sizes is expected to yield a parabolic shrinking rate [*Proussevitch et al.*, 1993b]

$$r_0^2 - r^2 \propto (t - t_0), \tag{35}$$

where r_0 is the bubble radius at time $t_0 < t$. This scaling between the shrinking rate and time is valid mostly for the early stage of the mass exchange, when the size of the small bubble has not changed significantly. In

©2013. American Geophysical Union. All Rights Reserved.

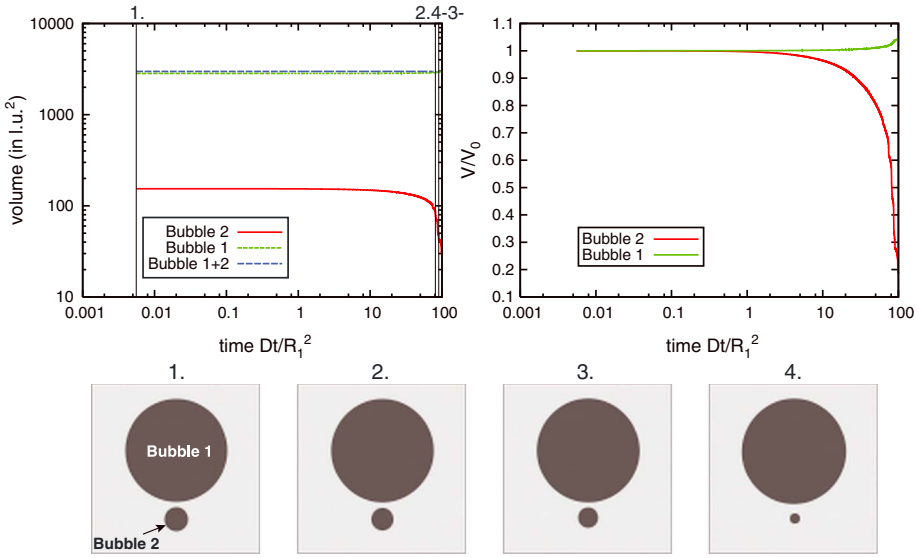

Figure 5. (a) Volume of each bubble during the mass exchange caused by Ostwald ripening between two bubbles (see evolution below). (b) Volume change for each of the bubbles as function of time. Each bubble's volume is normalized to its initial volume.

Figure 6, we compare the numerical results for the evolution of the small bubble size with the scaling above and find agreement for the first stage of the calculation. The latter stage of the calculation is marked by a faster shrinking rate that is caused by two effects. While the bubble's volume decreases, the boundary of the small bubble recedes faster than the large bubble boundary advances, because of the different surface to volume ratios of the two bubbles. This leads to a change in film thickness that affects the idealized parabolic shrinking law. The second effect is merely numerical; when the shrinking bubble becomes small, the spatial resolution becomes more limited and the results less accurate.

5.2. Calibration of the Model for Coalescence With Laboratory Experiments

During bubble coalescence, a melt film separating the bubbles drains and shrinks until a critical thickness (δ_{crit}) is reached and the film suddenly ruptures. Capturing the exact physics of this phenomenon is impossible from the numerical point of view, because the complex dynamics in the film occurs ultimately at scales significantly smaller than the effective radius of the bubbles ($\delta_{crit} \sim 10^{-7}$ m), and the dynamics of the film rupture is much faster than the drainage and poorly constrained. The model we propose offers two advantages over standard multiphase lattice Boltzmann models where bubble coalescence occurs automatically when the two free surfaces approach each other to within a computational grid cell. First, the mass conservation during the drainage of film fluid is resolved locally to a subgrid-scale (equation (10)). Second, and most importantly, an additional pressure term is introduced in the stress boundary condition at each free surface to account for the interaction between neighbor free surfaces, the disjoining pressure equation (14). The disjoining pressure term is expected to become significant for surfactant-rich interfaces, where foams can become stable over much longer timescales. We use c_Π as a free parameter to account for the subgrid effects of lubrication forces on the stabilization of the film prior to rupture.

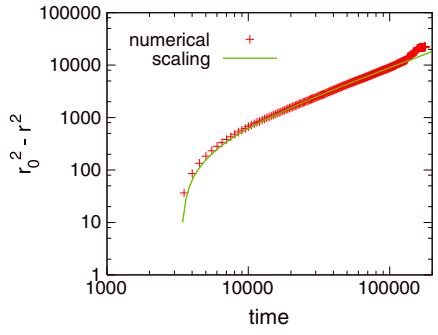

Figure 6. Comparison between the numerical results for the small bubble radius change with time. The early trend is in good agreement with a parabolic law, as expected. See the text for more details.

In order to calibrate the disjoining pressure term, we designed the simplest experiment that accounts for two approaching and distinct free surfaces:

©2013. American Geophysical Union. All Rights Reserved.

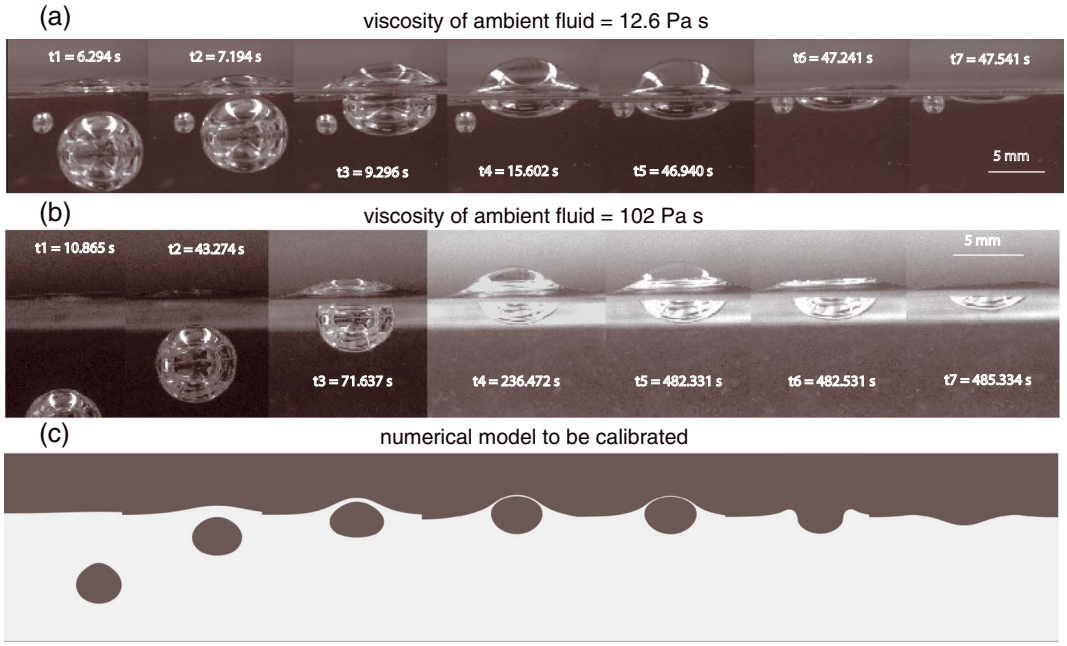

Figure 7. Examples of sequences of photographs taken during the bubble rise and film drainage in two experiments and comparison with snapshot from one of our numerical simulation (Figure 7c). The numerical simulation shows the typical results we obtain, the bubble rises, reaches a steady velocity, and decreases quickly as it approaches the free surface and film drainage starts until it ruptures. These calculations are used to constrain the disjoining pressure term over a range of Bond number by matching the duration of the film drainage with corresponding experiments.

a bubble approaching and bursting at a free surface. Different flow configurations (shear flows) or different regimes for the balance between hydrodynamic forces (presence of inertia at high Reynolds number) would require different experimental studies to build a more general parameterization. For instance the pressure at the free surface is fixed whereas for two colliding bubbles lubrication effect may become more important during the deformation of the interfaces. In this study, we use the laboratory procedure described in *Nguyen et al.* [2013], where air bubbles are injected into silicon oil (using a range of oil viscosity) and rise to a free surface. We used these experiments to calibrate the disjoining pressure dependence on the Bond number $\mathrm{Bo} = \Delta\rho g R^2/\sigma$. Figure 7 shows a visual comparison between two selected experiments and a numerical calculation with our free surface model. The duration of the film drainage between the bubble and the free surface was measured over a range of bubble radii. In the experiments, the flow regime is viscous, i.e., inertial forces are negligible. The reader is referred to *Nguyen et al.* [2013] for a thorough description of the experimental setup. The experiments revealed the existence of two regimes of film drainage at low *Re*, depending on the balance between buoyancy and surface tension stresses (Bond number). At $\mathrm{Bo} < 0.25$, in the capillary-dominated regime, the film drainage is caused by surface tension, and the characteristic timescale for drainage was found theoretically and experimentally to be

$$t_c = C_c \ln\left(\frac{\delta_0}{\delta_{\mathrm{crit}}}\right)\frac{\mu R}{\sigma}, \tag{36}$$

where σ is the surface tension between the two immiscible fluids, R the effective bubble radius, μ the dynamic viscosity of the ambient fluid, δ_0 the initial film thickness (before drainage), and C_c a constant which value was found experimentally to be about 20 [*Debregeas et al.*, 1998; *Nguyen et al.*, 2013]. The ratio $\delta_0/\delta_{\mathrm{crit}}$ was estimated from natural samples to be of the order of 10^2 to 10^3, as measured on natural samples with scanning electron microscopy or interferometry, for example [*Klug and Cashman*, 1996; *Debregeas et al.*, 1998].

As buoyancy stresses become more important ($\mathrm{Bo} > 0.25$), the drainage regime is governed by the balance between buoyancy and viscous stresses. The drainage time is then

$$t_g = C_g \ln\left(\frac{\delta_0}{\delta_{\mathrm{crit}}}\right)\frac{\mu}{\Delta\rho g R} = \frac{C_g}{C_c}\,\mathrm{Bo}\,t_c, \tag{37}$$

©2013. American Geophysical Union. All Rights Reserved.

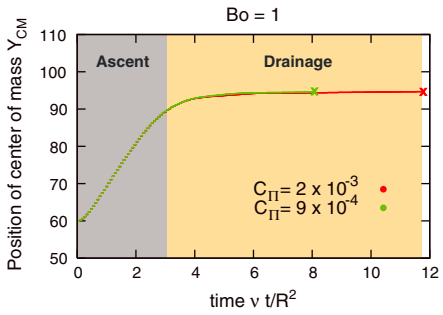

Figure 8. Vertical position of the bubble center of mass as function of time for Bo = 1 and two different choices of disjoining pressure constant c_Π. The longetivity of the bubble increases with c_Π. The crosses mark the end of the film drainage and the coalescence of the bubble with the free atmosphere.

where $\Delta\rho$ is the density difference between the bubble and the ambient fluid. The two empirical constant C_c and C_g were found experimentally to be 20 and 5, respectively.

The same general setup was used for the numerical calculations, a buoyant bubble is initially emplaced about 10 bubble radii below the unperturbed free surface. We compute the bubble's ascent, deceleration as it approaches the free surface and record the drainage time leading to the bubble rupture at the surface. The drainage time is defined similarly between the experiment and the calculations, it consists of the time interval between the sharp slowdown of the bubble as it approaches the free surface (the center of mass decelerates from a velocity close to the free ascent velocity for the bubble to rest) and the rupture of the film when it reaches its critical thickness δ_{crit}.

The disjoining pressure defined in equation (16) includes two constants c_Π and the range of the interaction between free surfaces d_{range}. The latter was fixed to a distance of three grid points, as in the study of *Koerner et al.* [2005]. We decided to keep d_{range} fixed and calibrate the disjoining pressure by varying the constant c_Π so as to reproduce the dimensionless drainage time observed experimentally over a range $0.1 \leq$ Bo ≤ 4, which overlaps both capillary- and gravity-driven drainage regimes. As expected, an increasing magnitude for c_Π yields a longer drainage time, as shown in Figure 8 at Bo = 1. The bubble slowing down as it interacts with the free surface and the subsequent film drainage leading to the bubble's rupture are clearly distinguished.

We repeated similar calculations over a range of Bo at different values of c_Π (Figure 9). We ran each calculation for about 200,000 iterations (in all case much longer than the expected experimental drainage time) to map the regime where coalescence occurred. We found that there is a critical disjoining pressure constant value where the two bubbles remained stable and that this value depends on Bo.

The experimental normalized drainage time was found to satisfy (Figure 10).

$$\frac{t_d}{t_x} = \begin{cases} 1 & \text{if Bo} < 0.25 \text{ and } x = c \\ 1 & \text{if Bo} > 0.25 \text{ and } x = g. \end{cases} \tag{38}$$

Figure 10b shows the best fit for c_Π to match the experimental results. Because of the two drainage regimes (below and above Bo = 0.25), the calibrated value for c_Π becomes

$$c_\Pi(\text{Bo}) = \begin{cases} 1.57 \times 10^{-3}\text{Bo} + 1.59 \times 10^{-5} & \text{if Bo} < 0.25 \\ 1.27 \times 10^{-4}\text{Bo}^{2.1} + 6.6 \times 10^{-4} & \text{if Bo} > 0.25. \end{cases} \tag{39}$$

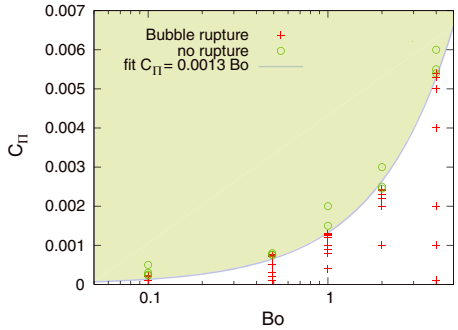

Figure 9. Regime diagram that shows how increasing disjoining pressures retard or sometimes prevent bubble rupture. All calculations presented here were run for a maximum of 200,000 iterations.

The correlations between c_Π and Bo established from the experiments of *Nguyen et al.* [2013] provide our model with an accurate treatment for the duration of the drainage of melt films between bubbles under capillary- and gravity-dominated regimes. Coalescence has deep implications for the mechanical behavior of a suspension and by extension for eruption dynamics. Our model is the first bubble dynamics model for magmatic suspensions to account for the complex dynamics associated with coalescence. The subgrid-scale physics of

©2013. American Geophysical Union. All Rights Reserved.

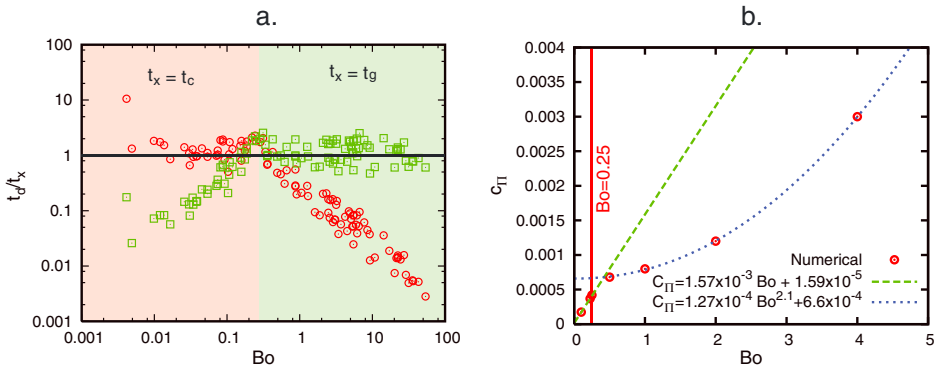

Figure 10. Functional form of the experimentally calibrated disjoining pressure—Bond number function. At Bo < 0.25 the trend is linear, it becomes nonlinear above 0.25. See the text for a more detailed discussion. (a) We show the same data set twice, with the drainage duration normalized first with the capillary-driven drainage timescale (red circles) and with a buoyancy-driven drainage timescale (green squares). (b) The best fit values for the disjoining pressure constant c_Π are shown for the whole range of Bond number. The two trends represent the two regimes observed in Figure 10a.

film drainage is parameterized and inserted as a pressure correction term through the disjoining pressure constant.

In the near future, we plan to conduct similar type of combined experimental-numerical effort to constrain the dependence of the disjoining pressure Π on the capillary number (shear to surface tension stresses). In the latter case, bubble deformation and its feedback into capillary stresses can significantly impact the film drainage rate during coalescence.

5.3. Sheared Suspensions

The effect of dispersed bubbles on the rheology of magmas has been studied theoretically and experimentally [*Manga et al.*, 1998; *Manga and Loewenberg*, 2001; *Stein and Spera*, 1992; *Stone*, 1994; *Taylor*, 1932]. It was found that the presence of bubbles induces a shear thinning behavior, i.e., the effective viscosity decreases with increasing strain rates. Bubbles influence on the effective viscosity are strongly controlled by the capillary number. At low Ca, when bubbles remain spherical because surface tension dominates the force balance at the scale of the bubbles, the effective viscosity is greater than for a melt with no bubbles. At large Ca (> 0.1), when bubbles can accommodate a substantial part of the deformation in the suspension, bubbles decrease the effective viscosity of the mixture. The importance of the suspension vesicularity has also been studied extensively and it was shown that the viscosity of the suspension increases weakly with vesicularity, at least in the limit of low vesicularity studied ($< 10\%$ in most cases). Here we discuss the effect of a constant imposed shear rate on a suspension, and more specifically, we focus on the deformation and orientation of these bubbles in response to an imposed simple shear.

The evolution of a sheared suspension is important because the rheology of the mixture is sensitive to the bubble size distribution, i.e., small bubbles can increase the effective viscosity of the mixture because of their resistance to deformation (low Ca), whereas large bubble will tend to accommodate most of the strain and therefore reduce the effective viscosity of the suspension. In this study, we explore the behavior of suspension over a range of imposed shear rates (we fix the initial bubble size, and hence the initial capillary number), but we do not account for degassing. The aim of these calculations is (1) to validate our bubble dynamics calculations under shear conditions with published theory and experiments for a single bubble and (2) to investigate the role of bubble interactions on the distribution of bubble shapes and orientations.

We present two sets of calculations. First, we compare and validate our numerical results for the steady shape and final orientation of a single bubble under simple shear conditions with theoretical and experimental results obtained by *Hinch and Acrivos* [1980], *Rallison* [1980], and *Rust and Manga* [2002a]. The second set of calculations aims at characterizing how the presence of other bubbles with the same size in a monodisperse suspension affects the distribution (average and standard deviation) of deformation and orientation in a suspension.

The LBM offers a very convenient approach to impose velocity boundary conditions on solid sites. We use the boundary condition of *Zou and He* [1997] to impose a velocity $(U_w, 0)$ at the lower wall and a standard bounceback of the distribution for the no-slip boundary condition on the top wall (see Figure 11). The

©2013. American Geophysical Union. All Rights Reserved.

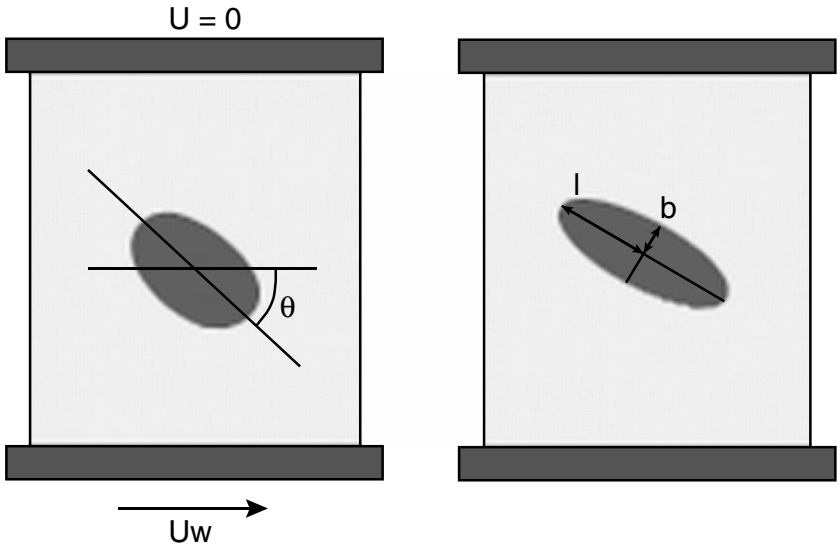

Figure 11. Illustration of the measurements used to characterize the bubble final orientation and shape. The actual bubbles shown here come from two calculations with Ca = (left) 0.2 and (right) 0.5.

missing distribution in melt sites adjacent to the lower boundary (moving wall) are f_2, f_5, and f_6, i.e., the distributions i with $\mathbf{e}_i \cdot \mathbf{n}_y > 0$, where $\mathbf{n}_y$ is the upward ($+y$) normal to the wall

$$\rho = f_0 + f_1 + f_3 + 2\left(f_4 + f_7 + f_8\right) \tag{40}$$

$$f_2 = f_4 \tag{41}$$

$$f_5 = f_7 + \frac{1}{2}\left(f_3 - f_1\right) + \frac{\rho U_w}{6} \tag{42}$$

$$f_6 = f_8 + \frac{1}{2}\left(f_1 - f_3\right) - \frac{\rho U_w}{6}. \tag{43}$$

The side boundary conditions are periodic. The capillary number, Ca, which represents the ratio of viscous to surface tension stresses is defined as

$$\mathrm{Ca} = \frac{\rho \nu U_w r}{H\sigma}, \tag{44}$$

where r is the initial bubble size, ρ and ν refer, respectively, to the melt density and kinematic viscosity [*Stone*, 1994]. If the Capillary number is identical for each bubble initially, coalescence will lead to a polydisperse bubble size distribution and therefore lead to a range of Ca in the suspension. In all our calculations, the domain is bounded on the sides by periodic boundaries and the whole system is oriented perpendicular to the direction of gravity (no buoyancy effect).

If the viscous stresses are negligible with respect to surface tension stresses ($\mathrm{Ca} \ll 1$), the bubble remains undeformed, that is spherical, and remains invariant under rotation. With increasing Ca, the bubble starts to deform and loses its spherical symmetry. The bubble therefore rotates until the drag force applied by the melt to the bubble balances surface tension. Note that we only consider flows where inertial forces can be neglected. The elongation of the bubble, once it reaches a steady shape, is often characterized by the dimensionless quantity

$$D = \frac{l - b}{l + b}, \tag{45}$$

where l and b are, respectively, the long and short semiaxis of the elliptic or pseudoelliptic final shape [*Hinch and Acrivos*, 1980; *Rust and Manga*, 2002a]. It is easy to see that $0 \leq D < 1$, where the two bounds hold, respectively, for an undeformed spherical bubble ($D = 0$) and an infinitely stretched bubble. Finally, the angle between the long axis of the bubble and the direction of the shear is defined as θ (see Figure 11 for an illustration of these definitions on results from calculations conducted at Ca = 0.2 and 0.5).

©2013. American Geophysical Union. All Rights Reserved.

5.3.1. Validation of the Model for the Deformation of a Single Bubble Under Simple Shear

At moderate Ca, i.e., Ca $< 10^3$, such as those expected under most magmatic conditions, bubbles are expected to reach a steady configuration and not break into smaller bubbles [*Bentley and Leal*, 1986; *Hinch and Acrivos*, 1980]. Moreover, at low Ca, i.e., Ca ≤ 0.5, the deformation of the bubble follows

$$D \simeq \mathrm{Ca} \tag{46}$$

as shown by *Taylor* [1932]. Under the same conditions (low Ca), the orientation of the bubble reaches

$$\theta = \frac{\pi}{4} - 0.6\mathrm{Ca}. \tag{47}$$

At greater Ca (≥ 1), *Hinch and Acrivos* [1980] derived theoretically that, once the bubble reaches a steady shape, the ratio of the elongated semiaxis of the bubble to its initial radius R follows

$$\frac{l}{R} \simeq 3.45\mathrm{Ca}^{1/2}, \tag{48}$$

which, assuming a 2-D elliptical bubble, yields

$$D \simeq \frac{11.9\mathrm{Ca} - 4}{11.9\mathrm{Ca} + 4}. \tag{49}$$

Similarly, they showed that, for large Ca, the orientation of the bubble at steady state is given by

$$\theta = \arctan\left(0.359\mathrm{Ca}^{-3/4}\right). \tag{50}$$

Rust and Manga demonstrated the validity of these relationship experimentally and pinned the transition from low to high Ca regimes to occur around Ca $= 0.5$.

To validate our model against these experimental and theoretical results, we ran simple shear calculations in a 200×100 grid points domain over a range of shear rate conditions ($0.1 \leq$ Ca ≤ 4). For each run, the bubble shape and orientation were measured at steady state. Our first test consists of a comparison between our numerical results, theory, and the laboratory experiments of *Rust and Manga* [2002a] for the shape and orientation of the bubble across a range of Ca. Figure 12 shows a very good agreement between both data sets and with equations (46) and (49). It is important to remember, however, that our calculations are limited at this stage to 2-D. As such, some of the small-scale discrepancies could be associated with the planar velocity field imposed by the 2-D symmetry in our calculations. The final orientation of the bubble in our simulations agrees very well with the experiments of *Rust and Manga* [2002a] and the scaling relationships presented in equations (47) and (50). We also find the transition between surface tension to viscous stress-dominated regime to be around Ca $= 0.5$, similarly to *Rust and Manga* [2002a]. Finally, the relationship between the deformation D of the bubble and its orientation θ also follows the experimental results of Rust and Manga. This gives us good confidence that our model captures accurately the stress balance at the interface between a bubble and the ambient melt.

5.3.2. Deformation and Orientation of a Monodisperse Suspension of Bubbles

We conducted similar simple shear flow calculations with a suspension of 20 bubbles with an initial radius of R. The initial position of each bubble was set randomly and we repeated each calculation at the given choice of Ca 3 times to assess the variability of our results with respect to random initial conditions. The goal of these calculations was to study the effect of other bubbles on the distribution of θ and D values over a range of capillary numbers and contrast the results with those for a single bubble.

In a suspension, the existence of a steady state is not guaranteed, especially when Ca becomes large, because shear promotes coalescence [*Okumura et al.*, 2006, 2009]. Coalescence affects the effective Ca of the suspension, as the average bubble radius increases at the detriment of the bubble number density. Therefore, instead of focusing on the steady deformation and orientation of the bubbles, we consider their temporal evolution parameterized in terms of the accumulated strain ($\epsilon = U_w t/H$) and measure the distribution of D and θ at a few discrete values of ϵ. This also allows us to compare the behavior of the suspension under different shear conditions. Whenever possible, we considered only calculations where coalescence was minimal and where the effect of bubbles on neighbor bubbles was mostly limited to the deformation of streamlines.

©2013. American Geophysical Union. All Rights Reserved.

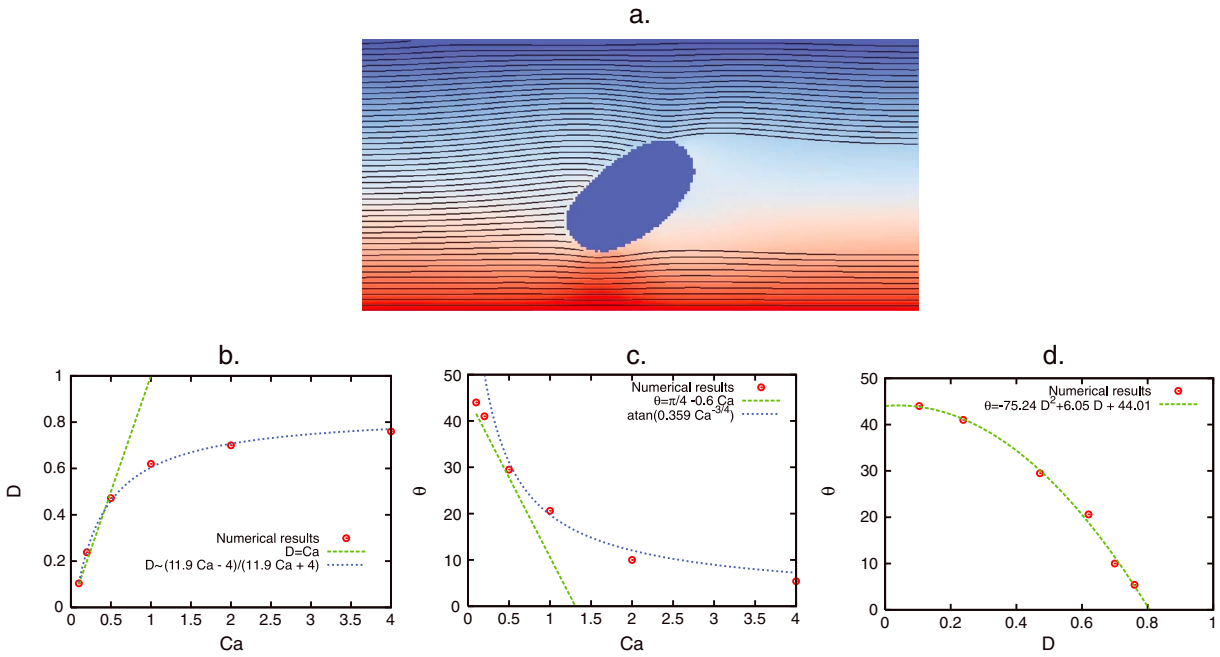

Figure 12. (a) Deformation of streamlines by the bubble (Ca = 0.5). (b) Results for the steady bubble shape D as function of Ca in our simple shear calculations. The dashed lines represent the theoretical trends and match closely the experimental results of Rust and Manga. (c) Same for θ and (d) for the correlation between the bubble's orientation and elongation.

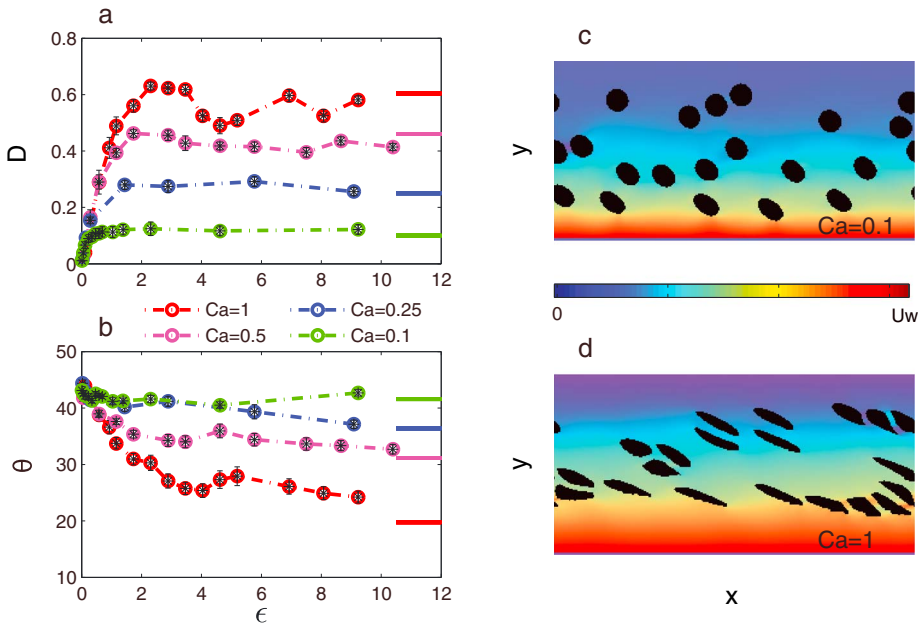

Figure 13. (a) Evolution of average deformation $\langle D \rangle_m$ of bubbles with strain accumulations under four different Ca (0.1, 0.25, 0.5, and 1). (b) Evolution of average orientation $\langle \theta \rangle_m$ of bubbles under the same Ca numbers as Figure 13a. Standard errors for each data points are also given in 13a and 13b. The solid lines at the right side mark the steady state $\langle D \rangle_m$ and $\langle \theta \rangle_m$ theoretical values for single bubble at specific Ca number. (c) Snapshot of multibubbles distribution and the ambient melt velocity field around bubbles for Ca = 0.1 at $\dot{\epsilon} \approx 6.923$. (d) Same as Figure 13c except for Ca = 1 at $\dot{\epsilon} \approx 6.923$. The wall velocity $\frac{U_W H}{\nu} = 0.0011731$ for Ca = 0.1, and $\frac{U_W H}{\nu} = 0.011731$ for Ca = 0.1.

©2013. American Geophysical Union. All Rights Reserved.

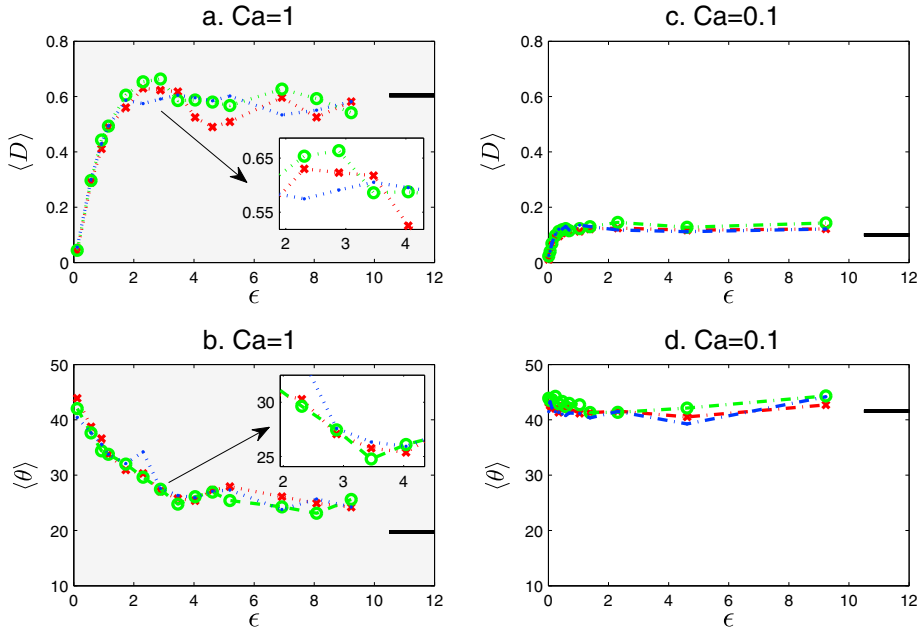

Figure 14. Evolution of average bubble shapes $\langle D\rangle_m$ and average bubble inclination angles $\langle\theta\rangle_m$ versus accumulated strain $\dot{\epsilon}$ with (a and b) Ca = 1 and (c and d) Ca = 0.1. The black solid lines at the right side mark their corresponding theoretical values for single bubble. In each panel, data points of different runs are marked by "x" in red, "o" in green, and "." in blue.

In Figure 13, we show the evolution of the average deformation $\langle D\rangle_m$ and average orientation $\langle\theta\rangle_m$ of the suspension over accumulated strain ϵ for Ca = 0.1, 0.25, 0.5, and 1, where

$$\langle D\rangle_m = \frac{1}{N_b}\sum_{k=1}^{N_b} D_k \tag{51}$$

$$\langle\theta\rangle_m = \frac{1}{N_b}\sum_{k=1}^{N_b} \theta_k, \tag{52}$$

and N_b is the total number of bubbles. Figures 13c and 13d illustrate the state of the suspension, the color coding shows the melt velocity at $\epsilon \approx 6.923$ for Ca = 0.1 and Ca = 1, respectively. The suspensions reach a quasi-steady state after $\epsilon \approx 2$–3 (Figures 13a and 13b). Steady state is defined as the state where the average bubble orientation and deformation in the suspension fluctuate around a constant value $\langle D\rangle$ and $\langle\theta\rangle$. At low Ca (< 0.5), when capillary stresses dominate, the steady state is characterized by $\langle D\rangle_m > D_s$, where m denotes multiple bubbles and s stands for a single bubble. At higher Ca, when viscous stresses dominate, we observe the opposite, which is $\langle D\rangle_m < D_s$. The average orientation $\langle\theta\rangle_m$ is greater than θ_s at high Ca. For Ca < 0.5, we do not observe a clear trend for the bubble's orientation as function of Ca and $\langle\theta\rangle_m$ seems not to have reached a well-defined steady state.

Because the number of bubbles $N_b = 20$ used in these calculations is modest and their initial spatial distribution are random, tested the reproducibility of our results by running three realizations for each set of calculation, each with different initial positions. A subset of these calculations (Ca = 0.1 and Ca = 1) are shown in Figure 14. For all Ca, the three realizations share similar trends for the average deformation and orientation of bubbles. The results are therefore reproducible and are expected to remain relevant even when starting with different spatial distributions of bubbles.

Our results for $\langle D\rangle_m$ suggest that bubbles deform less in a suspension than a single bubble at Ca above 0.5, whereas the deformation in the suspension exceeds predictions from a single bubble at Ca < 0.5. Bubble volume fraction Φ, which is fixed in our suspension calculations at $\Phi \approx 0.14$, as well as bubble shape and orientation can affect the effective Ca^* of bubbles in a suspension by influencing the effective viscosity ν^* of the multiphase mixture. From equation (44), the effective Ca^* of bubbly suspension can be defined as

$$\mathrm{Ca}^* = \frac{\rho\nu^* U_w r}{H\sigma}. \tag{53}$$

©2013. American Geophysical Union. All Rights Reserved.

Previous studies have shown that, at low Reynolds number (*Re*), suspensions with Ca in the range of (0, O(1)) are shear thinning, i.e., the effective viscosity ν^* decreases when the strain rate $\dot{\epsilon}$, and therefore, Ca increases [*Frankel and Acrivos*, 1970; *Han and King*, 1980; *Manga et al.*, 1998; *Rust and Manga*, 2002b]. To characterize the rheology of a suspension, it is common to use the relative viscosity ν_r, defined as the ratio of ν^* to the viscosity of the ambient melt ν. *Rust and Manga* [2002b] used laboratory experiments to quantify the decrease in relative viscosity of suspensions with increasing Ca. The relative viscosity is greater than unity at low Ca ($0 < \mathrm{Ca} < \mathrm{Ca}_c$), where the critical value Ca_c is estimated to be around 0.5–0.7 [*Rust and Manga*, 2002b]. At low Ca, bubbles remain spherical and the effective viscosity increases with Φ, because the deformed streamlines provide a net increase of viscous dissipation, which is not compensated by the increasing volume fraction of quasi inviscid bubbles [*Manga et al.*, 1998]. On the other end, at high Ca, elongated bubbles tilt almost horizontally providing less resistance to the flow of ambient melt. In addition, deformed bubbles can slide over each other, which, because of their low viscosity, helps to reduce viscous dissipation. Our results are in excellent agreement with these observations.

6. Conclusions

We have developed a new bubble growth model in magmas, which accounts for bubble-bubble interactions in a melt at rest or during flow. It is designed to obtain a more accurate description of the dynamics of bubbles during magma ascent. The model is based on the lattice Boltzmann model for flows with free surfaces and augmented with a decompression algorithm, to model the growth of bubbles by mechanical expansion and diffusion. The model was validated against analytical solutions and published results from bubble growth studies. Our new model constitutes a significant advance in our ability to model magmatic processes, because it accounts for the complex nonlinear hydrodynamic interactions between bubbles under different flow regimes.

We showcased the capabilities of our new model by investigating the complex interactions between bubbles of different sizes during Ostwald ripening and during shear flow. The model reproduces expected scalings for Ostwald ripening, demonstrating the ability to model mass transfer of dissolved volatiles between bubbles of different sizes. The shear flow calculations for a single bubble accurately reproduced existing theoretical and empirical results, confirming the accurate representation of viscous coupling between bubble and melt. Shear deformation of a suspension resulted in that a smaller average bubble deformation than for a single bubble when $\mathrm{Ca} > 0.5$ and the opposite for $\mathrm{Ca} < 0.5$.

Constraining the dynamical conditions in a volcanic conduit from erupted pumices does require models that can solve for the complex viscous coupling between the melt and exsolved gas phase. This model will enable us to study how bubble deformation affects growth by exsolution under shear flow conditions, which is not possible with the existing bubble dynamics model in volcanology. Bubble deformation leads to a greater interfacial area for the melt and exsolved volatiles which can promote faster degassing than expected from the models of *Gaonac'h et al.* [1996], *Lensky et al.* [2004], *L'Heureux* [2007], *Lyakhovsky et al.* [1996], *Proussevitch et al.* [1993a], *Proussevitch and Sahagian* [1998], and *Toramaru* [1995]. Our new model will also offer the opportunity to quantify the resultant drag and lift forces between a suspension and the melt in shear flow conditions, the dependence of the coalescence rate in a suspension as function of shear at constant and time-dependent (growth) vesicularity and introduce water-dependent viscosity and diffusivity. The ultimate objective behind the development of these numerical investigation of bubble dynamics is to provide conduit flow models with a parameterization of bubble-melt interactions that covers a wide range of dynamical conditions and vesicularity.

Notation

A	surface area of gas-melt interface surfaces.
Bo	Bond number.
c_Π	amplitude of the disjoining pressure.
c_Π	lattice speed in LBM model.
C	concentration of dissolved water content.
C_b	concentration of dissolved water content at the bubble-melt interface.
d_{range}	range of the disjoining pressure.
d_{int}	distance between interacting interfaces neighbor objects.
D	parameter of deformation of bubbles.

©2013. American Geophysical Union. All Rights Reserved.

D_{H_2O}	diffusion coefficient of the dissolved volatile.
$\mathbf{e}_i$	lattice velocity in *i* direction of LBM model.
f_i	distribution function in *i* direction of D2Q9 model.
F_i	body force in *i* direction on f_i.
g_i	distribution function in *i* direction of D2Q4 model.
G	Gibbs free energy.
H	distance between two walls in simulation model of shear effect on bubbles.
n	moles of gas molecules.
p_g	gas pressure.
r	bubble radius.
R	ideal gas constant.
S	Sieverts constant.
t	time.
t_{dec}	decompression timescale.
t_{vis}	viscosity timescale.
t_c	drainage time (Bo $<$ 0.25).
t_g	drainage time (Bo $>$ 0.25).
t_d	experimental normalized drainage time.
T	temperature.
U_w	bottom wall velocity in simulation model of shear effect on bubbles.
V	gas volume.
w_i	lattice weights in LBM model.
δ	critical thickness of the melt film between bubbles.
δ_i	initial melt film thickness.
Δ_ρ	density difference between the bubble and the ambient fluid.
ϵ	strain.
$\dot{\epsilon}$	strain rate.
κ	curvature of gas-melt interface.
μ	dynamic viscosity.
ν	kinetic viscosity.
Π	disjoining pressure.
ρ	density.
σ	surface tension.
τ_F	relaxation time for melt in LBM model.
τ_G	relaxation time for gas in LBM model.
θ	orientation of bubbles, angle between the long axis of bubble and the shear flow.

Acknowledgments
We thank E. Attar and C. Koerner for allowing us to obtain a copy of their LB model. We thank the editor as well as one anonymous reviewer for their constructive comments. The authors would like to acknowledge support from the National Science Foundation under grants NSF EAR 1250441 (for C.H., Y.S. and J.D) and NSF EAR 1250441(for C.N. and H.G.).

References

Attar, E., and C. Koerner (2009), Lattice Boltzmann method for dynamic wetting problems, *J. Colloid Interface Sci.*, *335*, 84–93, doi:10.1016/j.jcis.2009.02.055.

Bhatnagar, P. L., E. P. Gross, and M. Krook (1954), A model for collision processes in gases. I. Small amplitude processes in charged and neutral one-component systems, *Phys. Rev.*, *94*(3), 511–525.

Bentley, B. J., and L. G. Leal (1986), An experimental investigation of drop deformation and breakup in steady, two-dimensional linear flows, *J. Fluid Mech.*, *167*, 241–283, doi:10.1017/S0022112086002811.

Blower, J. D., J. P. Keating, H. M. Mader, and J. C. Phillips (2001), Inferring volcanic degassing processes from vesicle size distributions, *Geophys. Res. Lett.*, *28*, 347–350, doi:10.1029/2000GL012188.

Burgisser, A., and J. E. Gardner (2004), Experimental constraints on degassing and permeability in volcanic conduit flow, *Bull. Volcanol.*, *67*, 42–56, doi:10.1007/s00445-004-0359-5.

Burnham, C. W. (1975), Water in magmas: A mixing model, *Geochim. Cosmochim. Acta*, *39*, 1077–1084, doi:10.1016/0016-7037(75)90050-2.

Debregeas, G., P. G. de Gennes, and F. Brochard-Wyart (1998), The life and death of "bare" viscous bubbles, *Science*, *279*, 1704–1707, doi:10.1126/science.279.5357.1704.

DeHoff, R. T. A. (1991), A geometrically general theory of diffusion controlled coarsening, *Acta Metal. Mater.*, *39*, 2349–2360, doi:10.1016/0956-7151(91)90016-T.

Frankel, N. A., and A. Acrivos (1970), The constitutive equation for a dilute emulsion, *J. Fluid Mech.*, *44*, 65–78, doi:10.1017/S0022112070001696.

Frisch, U., B. Hasslacher, and Y. Pomeau (1986), Lattice-gas automata for the Navier-Stokes equation, *Phys. Rev. Lett.*, *56*, 1505–1508, doi:10.1103/PhysRevLett.56.1505.

Gaonac'h, H., S. Lovejoy, and S. Schertzer (2005), Scaling vesicle distributions and volcanic eruptions, *Bull. Volcanol.*, *67*, 350–357, doi:10.1007/s00445-004-0376-4.

©2013. American Geophysical Union. All Rights Reserved.

Gaonac'h, H., S. Lovejoy, J. Stix, and D. Scherzter (1996), A scaling growth model for bubbles in basaltic lava flows, *Earth Planet. Sci. Lett.*, *139*, 395–409, doi:10.1016/0012-821X(96)00039-8.

Gardner, J. E., M. Hilton, and M. R. Carroll (1999), Experimental constraints on degassing of magma: Isothermal bubble growth during continuous decompression from high pressure, *Earth Planet. Sci. Lett.*, *168*, 201–218, doi:10.1016/S0012-821X(99)00051-5.

Gardner, J. E., M. Hilton, and M. R. Carroll (2000), Bubble growth in highly viscous silicate melts during continuous decompression from high pressure, *Geochim. Cosmochim. Acta*, *64*, 1473–1483, doi:10.1016/S0016-7037(99)00436-6.

Gonnermann, H. M., and M. Manga (2003), Explosive volcanism may not be an inevitable consequence of magma fragmentation, *Nature*, *426*, 432–435, doi:10.1038/nature02138.

Gonnermann, H. M., and M. Manga (2007), The fluid mechanics inside a volcano, *Annu. Rev. Fluid Mech.*, *39*, 321–356, doi:10.1146/annurev.fluid.39.050905.110207.

Han, C. D., and R. G. King (1980), Measurement of the rheological properties of concentrated emulsions, *J. Rheol.*, *24*, 213–237, doi:10.1122/1.549562.

Higuera, F. J., S. Succi, and R. Benzi (1989), Lattice gas dynamics with enhanced collisions, *Europhys. Lett.*, *9*, 345–349, doi:10.1209/0295-5075/9/4/008.

Hinch, E. J., and A. Acrivos (1980), Long slender drops in a simple shear flow, *J. Fluid Mech.*, *98*, 305–328, doi:10.1017/S0022112080000171.

Klug, C., and K. V. Cashman (1996), Permeability development in vesiculating magmas: Implications for fragmentation, *Bull. Volcanol.*, *58*, 87–100, doi:10.1007/s004450050128.

Koerner, C., M. Thies, T. Hofmann, N. Thurey, and U. Rude (2005), Lattice Boltzmann model for free surface flow for modeling foaming, *J. Stat. Phys.*, *121*, 179–196, doi:10.1007/s10955-005-8879-8.

L'Heureux, I. (2007), A new model of volatile bubble growth in a magmatic system: Isobaric case, *J. Geophys. Res.*, *112*, B12208, doi:10.1029/2006JB004872.

Larsen, J. F., and J. E. Gardner (2000), Experimental constraints on bubble interactions in rhyolite melts: Implications for vesicle size distributions, *Earth Planet. Sci. Lett.*, *180*, 201–214, doi:10.1016/S0012-821X(00)00166-7.

Larsen, J. F., and J. E. Gardner (2004), Experimental study of water degassing from phonolite melts: Implications for volatile oversaturation during magmatic ascent, *J. Volcanol. Geotherm. Res.*, *134*, 109–124, doi:10.1016/j.jvolgeores.2004.01.004.

Larsen, J. F., M. H. Denis, and J. E. Gardner (2004), Experimental study of bubble coalescence in rhyolitic and phonolitic melts, *Geochim. Cosmochim. Acta*, *68*, 333–344, doi:10.1016/S0016-7037(03)00412-5.

Lautze, N. C., T. W. Sisson, M. T. Mangan, and T. L. Grove (2011), Segregation gas from melt: An experimental study of the Ostwald ripening of vapor bubbles in magmas, *Contrib. Mineral. Petrol.*, *161*, 331–347, doi:10.1007/s00410-010-0535-x.

Lensky, N. G., O. Navon, and V. Lyakhovsky (2004), Bubble growth during decompression of magma: Experimental and theoretical investigation, *J. Volcanol. Geotherm. Res.*, *129*, 7–22, doi:10.1016/S0377-0273(03)00229-4.

Lifshitz, I. M., and V. V. Slyozov (1961), The kinetics of precipitation from supersaturated solid solutions, *J. Phys. Chem. Solids*, *19*, 35–50, doi:10.1016/0022-3697(61)90054-3.

Liu, Y., and Y. Zhang (2000), Bubble growth in rhyolitic melt, *Earth Planet. Sci. Lett.*, *181*, 251–264, doi:10.1016/S0012-821X(00)00197-7.

Lyakhovsky, V., S. Hurwitz, and O. Navon (1996), Bubble growth in rhyolitic melts: Experimental and numerical investigation, *Bull. Volcanol.*, *58*, 19–32, doi:10.1007/s004450050122.

Manga, M., and M. Loewenberg (2001), Viscosity of magmas containing highly deformable bubbles, *J. Volcanol. Geotherm. Res.*, *105*, 19–24, doi:10.1016/S0377-0273(00)00239-0.

Manga, M., J. Castro, K. V. Cashman, and M. Loewenberg (1998), Rheology of bubble-bearing magmas, *J. Volcanol. Geotherm. Res.*, *87*, 15–28, doi:10.1016/S0377-0273(98)00091-2.

Mangan, M., K. V. Cashman, and S. Newman (1993), Vesiculation of basaltic magma during eruption, *Geology*, *21*, 157–160, doi:10.1130/0091-7613(1993)021<0157:VOBMDE>2.3.CO;2.

Mangan, M., and K. V. Cashman (1996), The structure of basaltic scoria and reticulite and inferences for vesiculation, foam formation, and fragmentation in lava fountains, *J. Volcanol. Geotherm. Res.*, *73*, 1–18, doi:10.1016/0377-0273(96)00018-2.

Mangan, M., and T. Sisson (2000), Delayed, disequilibrium degassing in rhyolite magma: Decompression experiments and implications for explosive volcanism, *Earth Planet. Sci. Lett.*, *183*, 441–455, doi:10.1016/S0012-821X(00)00299-5.

Navon, O., A. Chekhmir, and V. Lyakhovsky (1998), Bubble growth in highly viscous melts: Theory, experiments, and autoexplosivity of dome lavas, *Earth Planet. Sci. Lett.*, *160*, 763–776, doi:10.1016/S0012-821X(98)00126-5.

Nemchin, A. A., L. M. Giannini, S. Bodorkos, and N. H. S. Oliver (2001), Ostwald ripening as a possible mechanism for zircon overgrowth formation during anatexis: Theoretical constraints, a numerical model, and its application to pelitic migmatites of the Tickalara Metamorphics, Northwestern Australia, *Geochim. Cosmochim. Acta*, *16*, 2771–2787, doi:10.1016/S0016-7037(01)00622-6.

Nguyen, C. T., H. M. Gonnermann, Y. Chen, C. Huber, A. A. Maiorano, A. Gouldstone, and J. Dufek (2013), Film drainage and the lifetime of bubbles, *Geochem. Geophys. Geosyst.*, *14*, 3616–3631, doi:10.1002/ggge.20198.

Okumura, S., M. Nakamura, and A. Tsuchiyama (2006), Shear-induced bubble coalescence in rhyolitic melts with low vesicularity, *Geophys. Res. Lett.*, *33*, L20316, doi:10.1029/2006GL027347.

Okumura, S., M. Nakamura, A. Tsuchiyama, T. Nakano, and K. Uesugi (2008), Evolution of bubble microstructure in sheared rhyolite: Formation of a channel-like bubble network, *J. Geophys. Res.*, *113*, B07208, doi:10.1029/2007JB005362.

Okumura, S., M. Nakamura, S. Takeuchi, A. Tsuchiyama, T. Nakano, and K. Uesugi (2009), Magma deformation may induce non-explosive volcanism via degassing through bubble networks, *Earth Planet. Sci. Lett.*, *281*, 267–274, doi:10.1016/j.epsl.2009.02.036.

Ostwald, W. (1897), "Studien über die Bildung und Umwandlung fester Körper" (Studies on the formation and transformation of solid bodies), *Z. Phys. Chem.*, *22*, 289–330.

Park, Y., and B. Hanson (1999), Experimental investigation of Ostwald-ripening rates of forsterite in the haplobasaltic system, *J. Volcanol. Geotherm. Res.*, *90*, 103–113, doi:10.1016/S0377-0273(99)00023-2.

Proussevitch, A., D. Sahagian, and A. Anderson (1993a), Dynamics of diffusive bubble growth in magmas: Isothermal case, *J. Geophys. Res.*, *98*, 22,283–22,307, doi:10.1029/93JB02027.

Proussevitch, A., D. Sahagian, and V. Kutolin (1993b), Stability of foams in silicate melts, *J. Volcanol. Geotherm. Res.*, *59*, 161–178, doi:10.1016/0377-0273(93)90084-5.

Proussevitch, A., and D. Sahagian (1998), Dynamics and energetics of bubble growth in magmas: Analytical formulation and numerical modeling, *J. Geophys. Res.*, *103*, 18,223–18,251, doi:10.1029/98JB00906.

Qian, Y. H., D. D'Humières, and P. Lallemand (1992), Lattice BGK models for the Navier-Stokes equation, *Europhys. Lett.*, *17*, 479–484, doi:10.1209/0295-5075/17/6/001.

©2013. American Geophysical Union. All Rights Reserved.

Rallison, J. M. (1980), Note on the time-dependent deformation of a viscous drop which is almost spherical, *J. Fluid Mech.*, *98*, 625–633, doi:10.1017/S0022112080000316.

Rust, A. C., and M. Manga (2002a), Bubble shapes and orientations in low *Re* simple shear flow, *J. Colloid Interface Sci.*, *249*, 476–480, doi:10.1006/jcis.2002.8292.

Rust, A. C., and M. Manga (2002b), Effects of bubble deformation on the viscosity of dilute suspensions, *J. Non-Newtonian Fluid Mech.*, *104*, 53–63, doi:10.1016/S0377-0257(02)00013-7.

Sparks, R. S. J. (1978), The dynamics of bubble formation and growth in magmas: A review and analysis, *J. Volcanol. Geotherm. Res.*, *3*, 1–37, doi:10.1016/0377-0273(78)90002-1.

Stein, D. J., and F. J. Spera (1992), Rheology and microstructure of magmatic emulsions: Theory and experiments, *J. Volcanol. Geotherm. Res.*, *49*, 157–174, doi:10.1016/0377-0273(92)90011-2.

Stone, H. A. (1994), Dynamics of drop deformation and breakup in viscous fluids, *Annu. Rev. Fluid Mech.*, *26*, 65–102, doi:10.1146/annurev.fl.26.010194.000433.

Suga, S. (2006), Numerical schemes obtained from lattice Boltzmann equations for advection diffusion equations, *Int. J. Mod. Phys. C*, *17*, 1563–1577, doi:10.1142/S0129183106010030.

Taylor, G. I. (1932), The viscosity of a fluid containing small drops of another fluid, *Proc. R. Soc. London, Ser. A*, *138*, 41–48, doi:10.1098/rspa.1932.0169.

Toramaru, A. (1989), Vesiculation process and bubble size distributions in ascending magmas with constant velocities, *J. Geophys. Res.*, *94*, 17,523–17,542, doi:10.1029/JB094iB12p17523.

Toramaru, A. (1995), Numerical study of nucleation and growth of bubbles in viscous magmas, *J. Geophys. Res.*, *100*, 1913–1931, doi:10.1029/94JB02775.

Verhoogen, J. (1951), Mechanics of ash formation, *Am. J. Sci.*, *249*, 729–739, doi:10.2475/ajs.249.10.729.

Wagner, C. (1961), Theorie der Alterung von Niederschlägen durch Umlösen (Ostwald-Reifung), *Z. Elektrochem. Ber. Bunsen Ges. Phys. Chem.*, *65*, 581–591, doi:10.1002/bbpc.19610650704.

Yamada, K., H. Emori, and K. Nakazawa (2008), Time-evolution of bubble formation in a viscous liquid, *Earth Planets Space*, *60*, 661–679.

Zhang, Y. (1999), A criterion for the fragmentation of bubbly magma based on brittle failure theory, *Nature*, *402*, 648–650, doi:10.1038/45210.

Zou, Q., and X. He (1997), On pressure and velocity boundary conditions for the lattice Boltzmann BGK model, *Phys. Fluids*, *9*, 1591–1598, doi:10.1063/1.869307.

©2013. American Geophysical Union. All Rights Reserved.